Calculation of ATP production rates using the Seahorse XF Analyzer

Brandon R. Desousa[1], Kristen K.O. Kim[1], Anthony E. Jones[1], Andréa B. Ball[1], Wei Y. Hsieh[2], Pamela Swain[3], Danielle H. Morrow[1], Alexandra J. Brownstein[4], David A. Ferrick[3], Orian S. Shirihai[4], Andrew Neilson[3], David A. Nathanson[1], George W. Rogers[3], Brian P. Dranka[3], Anne N. Murphy[5], Charles Affourtit[6], Steven J. Bensinger[2], Linsey Stiles[1,4], Natalia Romero[3], and Ajit S. Divakaruni[1,7]

[1]Department of Molecular and Medical Pharmacology, University of California, Los Angeles, Los Angeles, CA 90095, USA

[2]Department of Microbiology, Immunology, and Molecular Genetics, University of California, Los Angeles, Los Angeles, CA 90095, USA

[3]Agilent Technologies, 5301 Stevens Creek Boulevard, Santa Clara, CA 95051, USA

[4]Department of Medicine, University of California, Los Angeles, Los Angeles, CA 90095, USA

[5]Cytokinetics Inc. 350 Oyster Point Blvd., South San Francisco, CA 94080, USA

[6]School of Biomedical Sciences, University of Plymouth, Plymouth PL6 8BU, United Kingdom

[7]Lead contact

Correspondence: adivakaruni@mednet.ucla.edu

ABSTRACT

Oxidative phosphorylation and glycolysis are the dominant ATP-generating pathways in mammalian metabolism. The balance between these two pathways is often shifted to execute cell-specific functions in response to stimuli that promote activation, proliferation, or differentiation. However, measurement of these metabolic switches has remained mostly qualitative, making it difficult to discriminate between healthy, physiological changes in energy transduction or compensatory responses due to metabolic dysfunction. We therefore developed a broadly applicable method to calculate ATP production rates from oxidative phosphorylation and glycolysis using Seahorse XF Analyzer data. We quantified the bioenergetic changes observed during macrophage polarization as well as cancer cell adaptation to *in vitro* culture conditions. Additionally, we detected substantive changes in ATP utilization upon neuronal depolarization and T cell receptor activation that are not evident from steady-state ATP measurements. This method generates a single readout that allows the direct comparison of ATP produced from oxidative phosphorylation and glycolysis in live cells. Additionally, the manuscript provides a framework for tailoring the calculations to specific cell systems or experimental conditions.

INTRODUCTION

ATP is critical for cellular energy transduction. Essential cellular functions such as maintenance of ion homeostasis, macromolecule biosynthesis, motility, and autophagy involve reactions coupled to ATP hydrolysis to support these otherwise energetically unfavorable processes. The two dominant ATP-producing pathways in mammalian cells are glycolysis and oxidative phosphorylation (Chandel, 2015). Glycolysis involves the cytoplasmic breakdown of one molecule glucose into two molecules of pyruvate, generating two molecules of ATP in the process. The fermentation of pyruvate to lactate and subsequent lactate efflux enables continuous glycolytic turnover. Pyruvate and other carbon-rich energy substrates such as fatty acids and amino acids can also be taken up by mitochondria and completely oxidized during oxidative phosphorylation. The chemical energy in these substrates is converted to potential energy by the mitochondrial respiratory chain, and this reservoir of potential energy is used to drive ATP synthesis (Rich & Maréchal, 2010; Nicholls & Ferguson, 2013).

It is now clear that redistributing the balance between oxidative phosphorylation and glycolysis can characterize – and in some cases determine – cell function and fate (Lunt & Vander Heiden, 2011; DeBerardinis & Chandel, 2020; Sullivan *et al*, 2018; Shin *et al*, 2020). Glycolysis and offshoot pathways play essential roles in generating precursors for macromolecule biosynthesis(Lunt & Vander Heiden, 2011), supporting one-carbon metabolism (Ducker & Rabinowitz, 2017), and establishing cytoplasmic reducing power (Lewis *et al*, 2014). Biological processes such as stem cell pluripotency(Gu *et al*, 2016), oncogenesis (DeBerardinis & Chandel, 2020), growth factor signaling (Pavlova & Thompson, 2016), and immune cell activation (Van den Bossche *et al*, 2017) are therefore frequently associated with a preferential shift towards glycolysis. Conversely, terminal differentiation is often accompanied by an increased capacity for oxidative phosphorylation and the complete oxidation of glucose and fatty acids (Chen *et al*, 2008; Wilson-Fritch *et al*, 2003; Divakaruni *et al*, 2014; Moyes *et al*, 1997; Hazim *et al*, 2022).

Despite the importance of cellular ATP production rates and the distribution between glycolysis and oxidative phosphorylation, common measurement approaches are often limiting. Snapshot measurements of cellular ATP content are routinely used to characterize changes in energy metabolism, but these are generally informative only in extreme cases of energetic dysfunction such as ischemia (Brand & Nicholls, 2011). During physiological cell activation, cells can readily increase the rate of ATP production to match the increased rate of consumption without appreciably changing steady-state ATP levels. A far more useful metric is the ATP:ADP ratio, reflecting the free energy change associated with ATP hydrolysis into ADP and inorganic phosphate. However, biochemical or mass spectrometry-based approaches to measure ATP:ADP are limited given that they are destructive measurements conducted on cell lysates and unable to measure real-time changes and are prone to experimental noise that masks subtle but meaningful differences. Kinetic measurements

of energy status are therefore extraordinarily specialized, requiring transfection of a genetically engineered ATP:ADP sensor and an expert understanding of the caveats when using molecular probes (Tantama & Yellen, 2014; Koveal *et al*, 2020). Importantly, all these approaches lack direct information about whether the measured ATP is derived from oxidative phosphorylation or glycolysis.

Fluorescence-based, multi-well technologies such as Seahorse XF Analysis can characterize these bioenergetic shifts, as simultaneous measurements of oxygen consumption rates (OCR) and extracellular acidification rates (ECAR) can gauge the relative balance between oxidative phosphorylation and glycolysis (Pelletier *et al*, 2014; Divakaruni & Jastroch, 2022) (i.e. OCR:ECAR ratio). However, precise quantification of the total rate of ATP production and the balance between these two pathways is not straightforward. Direct comparison is precluded by differences in unit scale between OCR (pmol O_2/min) and ECAR (mpH/min). Direct, quantitative comparison between the two pathways is further confounded by the differential ATP yields from each pathway: for oxidation of one molecule of glucose, the maximum glycolytic yield is 2 ATP as opposed to 33.45 ATP for oxidative phosphorylation (Mookerjee *et al*, 2017). As such, a large increase in acidification of the extracellular medium may not necessarily indicate a rebalancing of ATP production if it is matched with even a marginal increase in oxygen consumption.

Additionally, ECAR measurements can be influenced by cellular processes other than lactate efflux that also result in a net acidification of the extracellular medium. Indeed, the main component of ECAR in two-dimensional cell culture systems is often glycolysis and fermentation (McConnell *et al*, 1992), reflecting the uptake of uncharged glucose and the release of anionic lactate. However, other acidifying reactions can contribute to the measured ECAR. For example, CO_2 evolution during oxidative metabolism (e.g. dehydrogenases of the TCA cycle or the pentose phosphate pathway) acidifies the medium after hydration and generation of bicarbonate ($CO_2 + H_2O \rightarrow H_2CO_3 \rightarrow H^+ + HCO^{3-}$). Additionally, specific cell types can release appreciable amounts of organic acids such as pyruvate (Hong *et al*, 2016), glutamate (Divakaruni *et al*, 2017), fatty acids (Thompson *et al*, 2010)that may be reflected in ECAR measurements. As such, the extracellular acidification rate cannot itself quantify lactate efflux (Newell *et al*, 1993; Gillies *et al*, 2008; Divakaruni *et al*, 2014).

We therefore developed a method to transform OCR and ECAR into rates of ATP production from oxidative phosphorylation and glycolysis. Although measurements of OCR and ECAR have become a central cell biology technique, the qualitative nature of the analysis makes it difficult to discriminate between healthy, physiological shifts in bioenergetic pathways or compensatory responses due to mitochondrial dysfunction. This method detailed here provides a solution to this challenge in a single, live cell readout estimating the total rate of cellular ATP production as well as its distribution between oxidative phosphorylation and glycolysis. Model parameters are formed with data from over 20 primary and immortalized cell lines, and the analysis detects substantive changes not evident from steady-state ATP measurements. Although a broadly similar approach heavily reliant

89 on reductionist systems has been previous used, the values obtained from this largely empirical
90 strategy sharply contrast previous work (Mookerjee *et al*, 2015).
91
92 **MATERIALS AND METHODS**
93 **Chemicals**
94 All chemicals were purchased from Sigma-Aldrich unless otherwise stated.
95 **Animals and primary cells**
96 All animal procedures were performed in accordance with the NIH Guide for the Care and
97 Use of Laboratory Animals, and approved by the UCLA Animal Research Committee (ARC-2020-
98 027).
99 *Murine bone marrow-derived macrophages (BMDMs)*
100 BMDMs were cultured as previously described (Hsieh *et al*, 2020). Briefly, macrophages were
101 isolated from femurs of male C57BL/6J mice (Jackson 000664) and maintained at 37°C in a
102 humidified 5% CO_2 incubator. Cells were treated with 3 mLs RBC lysis buffer (Sigma-Aldrich) to
103 remove red blood cells for 5 minutes, centrifuged at 386*g* for 5 minutes, and resuspended in BMDM
104 culture medium. Culture medium consisted of high-glucose DMEM (Gibco 11965) supplemented with
105 10% heat-inactivated fetal bovine serum (FBS), 2 mM L-glutamine, 100 U/ml penicillin, 100 µg/mL
106 streptomycin, 500 µM sodium pyruvate, and 5% (v/v) conditioned medium containing macrophage
107 colony stimulating factor (M-CSF) produced by CMG cells to induce differentiation to BMDMs.
108 BMDMs were allowed to differentiate for 6 days, changing medium after four days, and then plated
109 for experiments.
110 *Rat cortical neurons*
111 Cortical neurons were generated from embryonic day 18 Sprague-Dawley rats as described
112 previously (Kushnareva *et al*, 2005) and maintained at 37°C in a humidified 5% CO_2 incubator. Cells
113 were plated onto poly-d-lysine-coated wells of black-walled 96-well plates for enzymatic assays or
114 Seahorse XF96 plates. Cells for 96-well plate-based assays were seeded at 2.5×10^4 cells/well and
115 maintained in maintenance medium composed of 200 µL Neurobasal (Thermo Fisher Scientific)
116 medium supplemented with 1X B27 serum-free supplement (Thermo Fisher Scientific), 2 mM
117 GlutaMAX (Thermo Fisher Scientific), 100 U/ml penicillin, and 100 µg/mL streptomycin. Half the
118 medium was replaced every 3–4 d. Experiments in 96-well plates were conducted at day in vitro (DIV)
119 13–17.
120 *Human T cells*
121 Frozen stocks of human naïve $CD4^+$ T cells were purchased from Lonza. Cells were thawed
122 and permitted to recover in RPMI 1640 (Gibco, #11875-085) supplemented with 10%(v/v) FBS at
123 37°C, 5% CO_2 for 18-24 hr. After recovery, cells were spun at 250*g* for 10 min and resuspended to a
124 final density of 4×10^6 cells/mL in Agilent Seahorse XF RPMI Medium pH 7.4 (# 103576-100)

125 supplemented with 10 mM glucose, 2 mM glutamine and 1 mM pyruvate (XF Assay Media). 50 µL of
126 the naïve T-cell suspension (2 x 10^5 cells) were plated in each well of a poly-D-lysine-coated Seahorse
127 XF96 microplate. Plates were spun at 200*g* for 1 min to adhere cells to the plate. 130 µL of warmed
128 XF Assay Media was then added to each well, and plates were either run in the XF Analyzer or used
129 to measure intracellular ATP concentration with the Cell-Titer Glo Assay (Promega). ATP
130 measurements were taken before and after activation with magnetic Dynabeads coated with anti-
131 CD3/CD28 antibodies (Thermofisher, 4:1 beads/cell).

132 *Additional primary cells preparations*

133 Neonatal rat ventricular myocytes (Rubio *et al*, 2009) and rat cortical astrocytes (Kim &
134 Magrané, 2011) were isolated as previously described. Murine splenocytes were isolated from
135 dissected spleens from C57BL/6 mice. Tissue was mechanically dissociated in HBSS and passed
136 through a 40 µm strainer. Cells were washed and resuspended in red blood cells lysis buffer (Stemcell
137 # 07850) and incubated on ice for 10 min. Cell were washed again in HBSS, passed through a 70
138 µm filter, counted, and used immediately. For Seahorse XF experiments cells were resuspended in
139 XF Assay Media and seeded at 1.5 x 10^5 cells/well.

140 *Mitochondrial Isolation*

141 Hearts from C57BL/6 mice were drained of blood and homogenized with a hand-held Polytron
142 followed by a Potter-Elvehjem Teflon-on-glass tissue grinder in ice-cold MSHE buffer [70 mM
143 sucrose, 210 mM mannitol, 5 mM HEPES, 1 mM EGTA, and 0.5% (w/v) fatty acid-free BSA](Kubli *et*
144 *al*, 2013). The homogenate was centrifuged at 500*g* for 10 minutes at 4°C. The supernatant was then
145 collected and centrifuged at 12,000 *g* for 10 minutes at 4°C to obtain a mitochondrial pellet. The pellet
146 was washed in MSHE and centrifuged at 12,000 *g* for 10 minutes at 4°C, and this wash step was
147 repeated. Finally, the pellet was resuspended in a small volume (~20 µL) of MSHE, and the protein
148 concentration was determined by Bradford assay.

149

150 **Cultured cells**

151 All cell lines were obtained from American Type Culture Collection (ATCC) and cultured as suggested
152 by the supplier except when otherwise notified. Each formulation of medium was supplemented with
153 10% (v/v) fetal bovine serum (FBS), 2 mM GlutaMAX, 100 U/mL penicillin, and 100 µg/mL
154 streptomycin unless otherwise specified. All cells were maintained at 37°C in a humidified 5% CO_2
155 incubator. Cell lines were maintained in the medium listed parenthetically: A549 [DMEM/F12 (Gibco
156 11330); HepG2 [MEM (Gibco 11095)]; HCT116 [RPMI (Gibco 11875), C2C12 [DMEM (Gibco 11960
157 + 2 mM glutamine + 1 mM pyruvate)], A431 [DMEM (Gibco 11960) + 2 mM glutamine + 1 mM
158 pyruvate), BAEC [DMEM (Gibco 11054)], BT474 [ATCC Hybri-Care Cat#46-x], H460 [RPMI (Gibco
159 11870), 1 mM HEPES, 4 mM glutamine, 5% FBS), HUVEC [EGM Endothelial Cell Growth Medium
160 (Lonza CC-3124)], Jurkat,[RPMI (Gibco A10491-01)], MCF7 [RPMI (Gibco 21870 + 2 mM glutamine

161 + 1 mM pyruvate)], MCF-10A [MEBM supplemented with Kit CC-3150 (Lonza) and 100 ng/mL cholera
162 toxin (Sigma)], MDA-MB231 [RPMI (Gibco 21870 + 2 mM glutamine + 1 mM pyruvate)], PC12 [RPMI
163 (ATCC 30-2001 + 2mM glutamine + 10% Horse Serum + 5% FBS], Raw 264.7 [DMEM (Gibco 11960)
164 + 2 mM glutamine + 1 mM pyruvate].

165 *3T3-L1 pre-adipocytes and differentiation*

166 3T3-L1 pre-adipocytes were maintained below ~70% confluency in DMEM (Gibco 11965)
167 supplemented with 10% (v/v) bovine calf serum (BCS), 100 U/mL penicillin, and 100 µg/mL
168 streptomycin. For differentiation, cells were plated on Day -2 and were allowed to reach confluency
169 over 48 hr. Differentiation was induced on Day 0 by addition of fresh medium with FBS replacing BCS
170 and supplemented with the following: 0.5 mM IBMX, 0.25 µM dexamethasone, 1 µg/ml insulin, and
171 100 nM rosiglitazone. On Day 2, medium was replaced to DMEM + FBS supplemented with only 1
172 µg/ml insulin, and thereafter insulin was removed when replacing medium every two days.

173 *Immortalized brown adipocytes*

174 Immortalized human brown adipocytes were maintained as described previously (Panic *et al*,
175 2020). Briefly, cells were cultured in DMEM supplemented with 25 mM glucose, 10% (v/v) fetal bovine
176 serum, 4 mM glutamine, 1 mM sodium pyruvate, 10 mM HEPES, and 100 U/ml penicillin with
177 100 µg/ml streptomycin. Cells were plated at $1x10^4$ cells/well and reached total confluency after
178 approximately 24 hr. Medium was then changed to induction medium consisting of the growth medium
179 as before supplemented with 1 µM rosiglitazone, 0.5 mM IBMX, 0.5 µM dexamethasone, 125µM
180 Indomethacin, 1 nM T3, and 4 nM human insulin. After two days, medium was changed to growth
181 medium supplemented with only rosiglitazone and insulin (concentrations as before), and this
182 medium composition was used to change the fluid every other day for an additional 5-6 days.

183

184 **Seahorse XF Analysis**

185 All oxygen consumption and extracellular acidification measurements were conducted using
186 an Agilent Seahorse XF96 or XF^{e}96 Analyzer. Experiments were conducted at 37°C and at pH 7.4
187 (intact cells) or 7.2 (isolated mitochondria). For experiments with cultured cells, only the inner 60 wells
188 were used, and the outer rim was filled with 200 µL of PBS throughout the incubation to minimize
189 variance in temperature and evaporative effects across the plate (Lundholt *et al*, 2003). All respiratory
190 parameters were corrected for non-mitochondrial respiration and background signal from the
191 instrument with addition of 200 nM rotenone and 1 µM antimycin A. Where appropriate, oligomycin
192 was used at 2 µM unless otherwise specified, and FCCP concentrations were titrated to determine
193 an optimal concentration for a given experiment. Unbuffered DMEM assay medium is composed of
194 DMEM (Sigma #5030; pH 7.4) supplemented with 31.6 mM NaCl, 3 mg/L phenol red, and 5 mM
195 HEPES unless otherwise indicated.

196 *XF analysis primary cortical neurons*

197 All experiments with primary cortical neurons were conducted in a custom, modified
198 Neurobasal-type medium (Divakaruni *et al*, 2017) rather than DMEM to maintain appropriate
199 osmolarity. Glutamine was omitted from the assay medium to minimize excitotoxic injury.

200 *Acid injections and calculation of buffering power*

201 Sequential injections of 62.5 nmol H^+ (25 µL of 1.25 mM H_2SO_4) were made using the
202 Seahorse XF injector ports into unbuffered DMEM assay medium (see above) supplemented with 8
203 mM glucose, 2 mM glutamine, 2 mM pyruvate and HEPES as indicated in the text. Values were
204 corroborated with matched experiments using 2.5 mM HCl made from freshly purchased stocks no
205 more than 2 months old. Calculations were made using a measurement microchamber volume of
206 2.28 µL. Step-by-step sample calculations for using the buffering power of the medium to convert
207 ECAR (mpH/min) to pmol H^+/min are provided in the Supplemental Worksheet.

208 *Calculation of lactate:H^+ and H^+:O_2*

209 Rates of medium acidification without contribution from respiration were calculated as follows:
210 DMEM assay medium was supplemented with 5 mM glucose and varying concentrations of 2-
211 deoxyglucose (2-DG) and 5 mM iodoacetate (IA) where indicated in the figure. Medium was also
212 supplemented with 200 nM rotenone (to block complex I), 1 µM antimycin A (to block complex III),
213 and 2 µM oligomycin (to block ATP hydrolysis and prevent an energy crisis). Rates were calculated
214 for 75 min, and the spent medium was immediately harvested from each plate and frozen at -80°C
215 for later calculation of lactate efflux by enzymatic assay (Mookerjee *et al*, 2015).

216 Rates of medium acidification in the absence of glycolysis were calculated as follows: DMEM
217 assay medium was supplemented with 5 mM pyruvate and 5 mM glutamine (no glucose was
218 provided) along with 2 mM 2-DG and 50 µM IA (to block residual glycolysis and glycogenolysis). 500
219 U/mL carbonic anhydrase was added to ensure rapid CO_2 hydration, though it was later determined
220 to have a negligible effect on rates of acidification. Respiratory rates were titrated by addition of
221 oligomycin, FCCP (500 nM or 1 µM), and rotenone with antimycin A. The medium was also
222 supplemented with varying concentrations of both UK5099 and BPTES (3 nM - 3 µM for both) to
223 further titrate the respiratory rate. Experiments with primary cortical neurons were conducted in
224 custom medium lacking glutamine as described earlier.

225 *Patient-derived glioblastoma cultures*

226 Patient-derived high-grade gliomas were isolated, purified, and maintained as cell lines or
227 implanted as orthotopic xenografts according to previously published protocols (Gosa *et al*, 2019).
228 Cultured cells (*in vitro*) and tumor cells acutely purified from xenografts (*ex vivo*) were seeded onto
229 Cell-Tak-coated XF96 plates (25 µg/well; Corning). Cells were plated at either 4.0×10^4 or 1.0×10^5
230 based on cell size and the initial oxygen consumption rate, and spun at 600*g* for 5 min to adhere cells
231 to the well.

232 *Cell activation assays*

233 Cortical neurons were plated at $2.5x10^4$ cells/well and acutely activated with 1.5 μM veratridine
234 added via the injector port of the instrument (Choi *et al*, 2009). Where indicated, cells were pretreated
235 with 2 nM ouabain immediately prior to the assay. When activating the NMDA receptor, 100 μM
236 NMDA was acutely given via the injector port to neurons with or without 15 min. pre-treatment of 10
237 μM MK-801. For these experiments, the custom assay medium was supplemented with 2 mM β-
238 hydroxybutyrate as substrate, as pyruvate could not be used due to complications with measuring
239 glutamate in the medium by a linked enzymatic assay to confirm depolarization and glutamate efflux
240 (data not shown). For acute, T cell activation, murine anti-CD3/CD28 Dynabeads (Gibco) were added
241 via the injector port as previously described (Gubser *et al*, 2013).

242 *LPS-mediated activation of BMDMs*

243 BMDMs were plated at $5.0x10^4$ cells/well for 48 hr. prior to cytokine treatment, which lasted
244 for 24 hr. unless otherwise specified. Lipopolysaccharide (LPS) was purchased from PeproTech, Inc.
245 (New Jersey, USA) and offered to cells at 50 ng/mL unless otherwise specified in the manuscript.

246 *H^+:O_2 in isolated heart mitochondria*

247 Isolated heart mitochondria were plated in XF96 plates (1.5 μg/well) and spun 2000*g* for 20
248 min to adhere mitochondria to the well. Assays were conducted in MAS medium ([220 mM mannitol,
249 70 mM sucrose, 10 mM KH_2PO_4, 5 mM $MgCl_2$, 1 mM EGTA, and 2 mM HEPES (pH 7.2)]
250 supplemented with 0.2% (w/v) fatty acid-free BSA. For all conditions, uncoupler-stimulated respiration
251 was measured in the presence of 2 μM oligomycin and 4 μM FCCP to eliminate effects of ATP
252 synthesis or hydrolysis on the acidification rate. Rates of respiration and acidification were measured
253 under three conditions: (i) pyruvate/malate (P/M): 10 mM pyruvate with 1 mM malate and 2 mM
254 dichloroacetate; (ii) pyruvate/malate with an inhibitor mix to block various enzymes to run a truncated
255 TCA cycle (P/M/truncated): 10 mM pyruvate with 1 mM malate, 2 mM dichloroacetate, 60 μM
256 fluorocitrate (to block isocitrate dehydrogenase), 2 mM malonate (to block succinate dehydrogenase),
257 and 1 mM aminooxyacetate (to block transaminase activity), and (iii) succinate/rotenone (S/R): 10
258 mM succinate with 2 μM rotenone to consume oxygen without release of CO_2 to acidify the
259 experimental medium(Mookerjee *et al*, 2015).

260 **Normalization of Seahorse XF assays to total protein or cell number**

261 Where indicated on the axis, Seahorse XF assays were normalized either to total protein or
262 cell number determined by *post hoc* high-content imaging. When measuring total protein, cells were
263 lysed in RIPA buffer [50 mM Tris, pH 7.4, 150 mM NaCl,1% (w/v) NP-40, 0.5% (w/v) sodium
264 deoxycholate, and 0.1% (w/v) sodium dodecyl sulfate], boiled, and assayed using the bicinchoninic
265 assay method (ThermoFisher).

266 When conducting *post hoc* cell counts, Seahorse XF plates were collected after assays,
267 washed with PBS, and fixed overnight with 2% (w/v) paraformaldehyde in PBS. Cells were left fixed
268 up to 2 weeks. On the day prior to counting, 10 ng/mL Hoescht 33342 (ThermoFisher) was added

269 and incubated overnight at 4°C. Cells were counted using a PerkinElmer Operetta high-content, wide-
270 field, fluorescence imaging system (ex./em. 361/497 nm) coupled to Columbus software (Operetta;
271 PerkinElmer, Waltham, MA, USA).

272 **Enzymatic lactate measurements**

273 Enzymatic lactate measurements were determined in the spent medium recovered after an
274 Agilent Seahorse XF assay. Medium was brought to room temperature if previously frozen, and mixed
275 1:1 with a 2X assay solution of 40 U/mL lactate dehydrogenase (Sigma-Aldrich L3916), 1 M Tris (pH
276 9.8), 20 mM EDTA, 40 mM hydrazine (Sigma-Aldrich 309400), and 4 mM NAD^+. The reaction velocity
277 was given by NADH fluorescence (ex./em. 340/460) and measured using a Tecan Spark multimode
278 plate reader (Mookerjee *et al*, 2015). Measurements were taken after 2-4 min (readings were taken
279 every 30 sec. to determine when stable values were achieved), and calibrated against known lactate
280 concentrations (Sigma-Aldrich L7022). Importantly, lactate standards were made in assay medium
281 matching the experimental medium to account for any effects from millimolar concentrations of
282 pyruvate in some experimental medium. Standard curves were calculated between 0.2 and 100.0
283 nmol lactate and modeled with a Michaelis-Menten curve using GraphPad Prism 5.0.

284 **ATP Content**

285 Cellular ATP content was measured in lysed cells with the Cell Titer Glo assay (Promega) in
286 96-well plates according to the manufacturer's specifications.

287 **Quantification and statistical analysis**

288 All statistical parameters, including the number of replicates (n), can be found in the figure
289 legends. Statistical analyses were performed using Graph Pad Prism 5 software for Mac OS X. Data
290 are presented as the mean ± SEM unless otherwise specified. Individual pairwise comparisons were
291 performed using two-tailed Student's t-test. For experiments involving two or more factors, data were
292 analyzed by one-way, repeated measures ANOVA followed by Dunnett post-hoc multiple
293 comparisons tests. Data were assumed to follow a normal distribution (no tests were performed).
294 Values denoted as follows were considered significant: *, $p < 0.05$; **, $p < 0.01$; ***, $p < 0.001$.

295

296 **RESULTS**

297 **<u>Development and Validation of the Method</u>**

298 The Seahorse XF Analyzer provides kinetic readouts of the oxygen consumption rate (OCR;
299 in pmol O_2/min) and extracellular acidification rate (ECAR; in mpH/min). These measurements very
300 often correlate with oxidative phosphorylation (OCR) and glycolysis (ECAR), but do not directly reflect
301 the quantity of ATP produced via each pathway. A strategy to convert OCR and ECAR readings into
302 rates of ATP produced from oxidative phosphorylation and glycolysis involved three principal steps:

303 (i) Transforming ECAR (mpH/min) into a proton production rate (pmol H^+/min) so rates of
304 medium acidification could be directly compared against rates of oxygen consumption
305 (pmol O_2/min) or lactate efflux (pmol lactate/min) with similar units.
306 a. mpH/min → pmol H^+/min
307 (ii) Accounting for sources of acidification not associated with glycolysis and fermentation
308 so changes in H^+ production quantitatively reflect lactate efflux.
309 a. pmol H^+/min → pmol $H^+_{Lactate}$/min
310 (iii) Converting rates of oxygen consumption and lactate efflux into ATP produced from
311 oxidative phosphorylation and glycolysis using established stoichiometry.
312 a. pmol O_2/min → pmol ATP_{OxPhos}/min
313 b. pmol $H^+_{lactate}$/min → pmol ATP_{Glyco}/min
314 c. pmol ATP/min = pmol ATP_{OxPhos}/min + pmol ATP_{Glyco}/min
315 The work presented uses a 96-well Seahorse XF Analyzer platform. Although some values
316 cannot be directly translated to 24-well instruments due to differences in volume of the measurement
317 microchamber, the experimental strategy to calculate these values is universal across all Seahorse
318 XF platforms.
319 (i) Transforming ECAR into a proton production rate
320 It was first necessary to convert ECAR into values of pmol H^+/min so rates of medium
321 acidification could be easily compared against OCR (in pmol O_2/min) and parallel lactate efflux assays
322 (in pmol lactate/min). This unit conversion required calculating the buffering power of the experimental
323 medium. Buffering power is defined here as the pH change in the measurement microchamber
324 elicited by a given amount of H^+ (Fig. 1A). Importantly, sequential additional of H_2SO_4 showed the
325 change in pH was directly proportional to the added H^+ over a range greater than 0.5 pH units (Fig.
326 1B). Predictably, as the concentration of HEPES in the medium increased, there was a smaller drop
327 in pH elicited from the added H^+. The results demonstrate that extracellular acidification
328 measurements in mpH/min are readily converted to values of pmol H^+/min by applying a scalar factor
329 accounting for the buffering power of the medium and the volume of the measurement microchamber.
330 Sample calculations and step-by-step instructions for transforming ECAR into values of pmol H^+/min
331 are provided in the first tab of the Appendix Worksheet available in the manuscript Appendix.
332
333 (ii) Accounting for sources of acidification other than lactate efflux
334 It was then necessary to determine whether measurements of H^+ efflux could indeed
335 accurately measure lactate efflux. In principle, there could be several reactions that could cause a
336 meaningful net pH change in the experimental medium in addition to the incomplete oxidation of
337 uncharged glucose into anionic lactate (Fig. EV1A). Other glycolysis-linked reactions can result in
338 medium acidification, such as the efflux of anionic pyruvate or CO_2 evolution during the oxidative

339 pentose phosphate pathway (Fig. EV1B). Additionally, several mitochondrial dehydrogenases will
340 generate CO_2 during the complete oxidation of energy substrates and oxidative phosphorylation.
341 These include the 2-oxoacid dehydrogenase family (pyruvate dehydrogenase, α-ketoglutarate
342 dehydrogenase, and the branched chain keto acid dehydrogenase) and isocitrate dehydrogenase
343 (Fig. EV1C). Furthermore, specific cell types may release organic acids under certain condition, such
344 as hepatocyte efflux of ketone bodies during robust fatty acid oxidation or neuronal release of
345 glutamate during prolonged depolarization.

346 Rather than attempt to account for every possible acidifying reaction, we began by testing the
347 hypothesis that respiratory acidification (CO_2 evolution from mitochondrial dehydrogenases linked to
348 O_2 consumption) would be the only acidifying process with a large enough flux to affect the
349 measurements on a scale comparable with lactate efflux in the basal state. If this hypothesis is
350 correct, then the following testable predictions should hold. First, if respiratory acidification is indeed
351 the only measurable source of non-glycolytic acidification, any remaining acid production should be
352 attributable to glycolysis when respiration is inhibited. Similarly, in the absence of glycolysis,
353 respiration should be directly proportional to the remaining acidification rate.

354 *In the absence of respiration, glycolysis is the exclusive source of measurable extracellular*
355 *acidification*

356 We first measured whether lactate efflux was directly proportional to H^+ production after
357 chemical inhibition of the respiratory chain. In the presence of electron transport chain inhibitors,
358 cellular H^+ production was gradually reduced with increasing concentrations of glycolytic inhibitors in
359 A549 cells (Fig. 1C). We then measured the lactate content in the spent experimental medium from
360 these samples using an enzymatic lactate assay (Fig 1D) to determine the relationship between
361 lactate efflux and acid production in the absence of respiration (Fig. 1E). As a negative control, no
362 measurable acidification was observed in cultured pancreatic β-cells(Zhao *et al*, 2001), which do not
363 express appreciable levels of lactate dehydrogenase or monocarboxylate transporter-1. Using 17
364 different cell types comprised of primary and immortalized cultures, this analysis yielded an average
365 lactate:H^+ ratio of 1.53 ± 0.12 (Fig. 1F; Appendix Table 1).

366 Unexpectedly, this value deviated substantially from our expectations and was substantially
367 different from previous efforts to correlate H^+ production and lactate efflux rates (Mookerjee *et al*,
368 2015). In principle, the lactate:H^+ ratio should never be greater than 1, since lactate efflux should
369 never exceed the total H^+ efflux given their 1:1 stoichiometry. In fact, the theoretical lactate:H^+ should
370 be less than 1 due to acidifying reactions associated with glycolysis but distinct from lactate efflux
371 (Fig. EV1B). We reasoned that this discrepancy could be due to the incomplete coverage of the
372 measurement well by the fluorometric sensor of the Seahorse XF cartridge: although the enzymatic
373 lactate measurements used medium collected from the entire well, outer portions of the well are likely

374 undetected by the fluorometric sensor spot(s) during the acidification measurements (Gerencser *et*
375 *al*, 2009) (Fig. EV2A).
376 To test this, we scraped cells from the measurement well from either the center of the three
377 risers directly under the sensor (creating a "donut" shape of cells in the well) or on the rim of the plate
378 outside the three risers (leaving cells in the center untouched) (Fig. EV2B). As predicted, both OCR
379 and ECAR were significantly reduced when cells in the middle of the well were removed, but losing
380 cells along the outer rim did not significantly affect the measurements (Fig. EV2C). To ensure the
381 results were not due to changes in cell number, the lactate:H^+ ratio was calculated for these
382 conditions. Consistent with the sensor not seeing the outer edges of the well, lactate:H^+ was lowered
383 close to 1 when cells were removed from the outer rim, and increased beyond 8 when cells were
384 removed from center of the plate (Fig. EV2D). Rather than a systemic error with the buffer capacity
385 or enzymatic measurements, the result demonstrates that incomplete sensor coverage of the
386 measurement well is a main driver of why lactate:H^+ values deviate from theoretical expectations.
387 *In the absence of glycolysis, respiration is the exclusive source of measurable medium*
388 *acidification*
389 Having shown that medium acidification is tightly correlated with glycolysis in the absence of
390 respiration in Figure 1, we then tested whether medium acidification would be tightly correlated to
391 respiration in the absence of glycolysis. We therefore measured acidification rates in HepG2 cells
392 offered glucose-free medium containing pyruvate, glutamine, and the glycolytic inhibitors 2-
393 deoxyglucose and iodoacetate. The rates of respiration and acidification were titrated by adjusting
394 flux through the electron transport chain (with oligomycin, FCCP, and rotenone with antimycin A) and
395 blocking substrate uptake and oxidation (with varying concentrations of the mitochondrial pyruvate
396 carrier inhibitor UK5099 and the glutaminase inhibitor BPTES) (Figs. 2A&B).
397 We observed a proportional relationship between respiration and medium acidification in the
398 absence of glycolysis (Fig. 2C). We again extended this analysis to a panel of 21 different primary
399 and immortalized cell preparations to yield an average H^+:O_2 ratio of 0.38 ± 0.05 (Fig. 2D; Appendix
400 Table 2). However, similarly to the values obtained for lactate:H^+, the composite H^+:O_2 again deviated
401 sharply from expectations and previous attempts to correct ECAR for respiratory acidification. The
402 value obtained was much lower than the theoretical H^+:O_2 of complete oxidation of either pyruvate
403 (0.80) or glutamine (0.67) (Mookerjee *et al*, 2015).
404 As such, we conducted a series of experiments to better understand the factors that shape
405 the H^+:O_2 value and whether experimental perturbations would change respiratory acidification in
406 expected ways. We first examined whether oxidation of different substrates would perturb H^+:O_2
407 values, as complete oxidation of various substrates yields varying H^+:O_2 ratios. Indeed, the H^+:O_2
408 ratio resulting from pure glutamine oxidation was fractionally lower than pure pyruvate oxidation (Figs.
409 EV3A-C).

410 We then further examined whether choice of respiratory substrates could influence $H^+:O_2$
411 ratios in isolated mitochondria, a simplified system where the experimental conditions are highly
412 controlled and metabolic reactions can be well defined. We tested acidification from uncoupled
413 respiration in rat heart mitochondria offered (i) pyruvate with malate (P/M), (ii) P/M and inhibitors of
414 multiple enzymes creating a truncated TCA cycle (P/M truncated) (Mookerjee *et al*, 2015), and (iii)
415 succinate with rotenone (S/R). The results qualitatively exhibited the expected behavior: the H^+/O_2
416 ratio for mitochondria oxidizing P/M increased in the presence of inhibitors which blocked downstream
417 TCA cycle reactions (e.g. the alkalinizing succinyl CoA synthetase reaction). Moreover, succinate
418 oxidation in the presence of rotenone, which will support oxygen consumption without generating
419 CO_2, shows robust respiratory rates with negligible changes in pH (Figs. EV3D,E).
420 However, even in this reductionist system, the measured $H^+:O_2$ fell far below expected values
421 (theoretical $H^+:O_2$ of P/M truncated = 1). We therefore used the XF24 system to further ensure that
422 the result was not a peculiarity of an individual instrument platform. Using the same workflow as
423 before, and accounting for the larger microchamber volume of the 24-well platform, nearly identical
424 results were observed where respiratory acidification in isolated mitochondria fell short of theoretical
425 predictions (Fig. EV3F).
426 Lastly, in addition to showing that respiratory substrates could affect the $H^+:O_2$ ratio, we
427 wanted to determine whether forced efflux of organic acids other than lactate could also affect the
428 measurements in predictable ways. For a proof-of-concept example, we measured whether NMDA-
429 induced efflux of glutamate would alter the $H^+:O_2$ in primary cortical neurons. Neurons were offered
430 exclusively β-hydroxybutyrate with glycolytic inhibitors, so lactate efflux or sources of glycolytic acid
431 production could not interfere with the measurements. As expected, NMDA-induced efflux of
432 glutamate in primary cortical neurons caused a pronounced spike in the acidification rate (Fig. EV3G)
433 and the $H^+:O_2$ ratio (Fig. EV3H) that was sensitive to the NMDA-receptor antagonist
434 MK801(Divakaruni *et al*, 2017). The result was not attributable to glycolysis, as lactate efflux was
435 negligible and unchanged across conditions (Fig. EV3I). Taken together, the demonstration that
436 H^+/O_2 ratios respond in expected ways to changes in substrate oxidation and non-glycolytic acid efflux
437 provided additional confidence in the accuracy of the measured values.
438
439 (iii) <u>Converting rates of oxygen consumption and lactate efflux into ATP produced from oxidative</u>
440 <u>phosphorylation and glycolysis</u>
441 The results from Figures 1 and 2 demonstrate that rates of H^+ production can, in principle,
442 quantify lactate efflux after correcting for respiratory acidification and accounting for the sensor
443 coverage of the plate well. We therefore transformed H^+ production rates into lactate efflux rates in
444 Equation 1 as follows:
445 **Eq. 1**: pmol lactate/min = $1.53 * (H^+_{Total} - 0.38 * OCR_{Mito.})$, where

446 - 1.53 = average lactate:H^+ value obtained in Fig. 1;
447 - H^+_{Total} = H^+ production rates read by the instrument;
448 - 0.38 = average H^+:O_2 value obtained in Fig. 2;
449 - $OCR_{Mito.}$ = basal mitochondrial respiration;

450 To validate whether these average values obtained under constrained conditions could be
451 broadly applied across different cell types under typical assay conditions (i.e. complete assay medium
452 with both glycolysis and oxidation phosphorylation functional), we compared lactate efflux calculated
453 using the XF Analyzer against an enzymatic assay in A549 adenocarcinoma cells, C2C12 myoblasts,
454 and murine BMDMs (Fig. 3A). Prior to adjusting the measurements as in Eq. 1, the H^+ production rate
455 underestimated the rate of lactate efflux (comparing leftmost bars in each graph with rightmost). But
456 as expected, correcting Seahorse XF measurements for respiratory acidification and sensor coverage
457 resulted in lactate efflux values (middle bars) that matched enzymatic measurements. Taken together
458 with Figure 1, the results suggest the consensus values and approximations used here should be
459 applicable across a broad range of cell types under normal assay conditions.

460 The ability to quantify lactate efflux with rates of H^+ production allows the transformation of
461 ECAR into a rate of ATP produced by glycolysis. All necessary parameters are obtained during
462 standard respirometry profiling (Figs. 3B & C), and sample calculations with representative data sets
463 are available in the Appendix Worksheet.

464 The rate of mitochondrial ATP production can be estimated by applying a P:O ratio (moles of
465 ADP phosphorylated per mole of oxygen consumed) to the respiration that drives ATP
466 synthesis(Brand, 2005), which is determined using sensitivity to the ATP synthase inhibitor
467 oligomycin. As detailed elsewhere, oligomycin-sensitive respiration will slightly underestimate ATP-
468 linked respiration (due to overestimating proton leak), though this is a small, ~10% overestimate
469 which can be adjusted ($0.1*OCR_{Leak}$ in Eq. 2) (Affourtit & Brand, 2009). Moreover, assumptions must
470 be made for the selection of P/O ratio based on which substrate is being oxidized. Here, we use a
471 value of P:O = 2.73 (P:O_2 = 5.45), the maximum value for complex I-driven respiration(Watt *et al*,
472 2010) and within the range of values for complete glucose oxidation(Mookerjee *et al*, 2017). The rate
473 of ATP from oxidative phosphorylation can therefore be estimated as in Eq. 2:

474 **Eq. 2**: $ATP_{OxPhos} = 5.45*(OCR_{ATP} + 0.1*OCR_{Leak})$

475 - 5.45 = P:O_2 (moles of ADP phosphorylated per O_2 consumed);
476 - OCR_{ATP} = ATP-linked respiration (respiration sensitive to oligomycin);
477 - OCR_{Leak} = Respiration associated with proton leak (respiration insensitive to
478 oligomycin);

479 The rate of glycolytic ATP production can be estimated with 1:1 stoichiometry to the lactate
480 efflux rate (**Eq. 1**), and the total ATP production rate is given by the sum of Eqs. 1 & 2. See Appendix
481 Worksheet for sample calculations

482 **Eq. 3**: $ATP_{Glyco.}$ = **Eq. 1**

483 **Eq. 4**: $ATP_{Total} = ATP_{OxPhos.} + ATP_{Glyco.}$

484 Notably, this calculation will slightly underestimate rates of glycolytic ATP, as it fails to account
485 for the ATP generated during glycolysis when glucose-derived pyruvate is funneled into mitochondria
486 for complete oxidation (Mookerjee *et al*, 2017). Accounting for this would require knowing (or
487 assuming) the fractional contribution of glucose oxidation to oxidative phosphorylation relative to
488 other substrates. To test whether this omission would appreciably affect experimental conclusions,
489 we measured rates of ATP production in A549 cells offered complete medium or a simple salts
490 medium supplemented with only glucose. Offering cells only glucose in simple salts allowed
491 calculation of this additional glycolytic ATP by applying known stoichiometry and assuming respiration
492 is exclusively driven by glucose oxidation with no contribution from endogenous substrate stores.
493 However, rates of both oxidative phosphorylation and uncoupler-stimulated respiration were
494 substantially limited when cells were offered medium containing solely glucose (Figs. 3D&E).
495 Additionally, rates of glycolytic ATP production between groups were only marginally altered despite
496 accounting for the cytoplasmic ATP production linked to mitochondrial glucose oxidation (Fig. 3D).
497 We therefore chose not to account for this component, favoring – on balance – an approach where
498 cells are offered complete DMEM to measure rates of oxidative phosphorylation and uncoupled
499 respiration that are not restricted by substrate limitation.

500 Lastly, prior to applying the method to various models of cell activation, we measured how
501 altered rates of organic acid efflux in response to activation stimuli may affect the measurements. We
502 chose adrenergic activation of brown adipocytes as a model system, as adipocyte lipolysis is known
503 to cause release of fatty acids into the experimental medium (Thompson *et al*, 2010). Figs. EV4A-C
504 show that stimulation of brown adipocytes with norepinephrine results in the hallmark increase in
505 uncoupled respiration, as well as an increased rate of H^+ production. To determine whether the
506 contribution of organic acid efflux was different upon norepinephrine stimulation, lactate efflux was
507 measured enzymatically from matched samples on the same Seahorse XF plate. As before,
508 comparing lactate efflux calculated from the XF Analyzer against that measured from an enzymatic
509 assay was within experimental error of multiple biological replicates (Fig. EV4D). However, it was
510 clear that non-glycolytic acid production was increased upon norepinephrine stimulation: the XF
511 Analyzer showed almost a two-fold increase in lactate production in response to adrenergic activation,
512 while the enzymatic assay measured only a 1.5-fold increase (Fig. EV4E). This suggests that H^+
513 measurements were somewhat confounded by efflux of organic acids distinct from lactate.
514

515 **Application of the Method**

516 *ATP production rates show patient-derived glioma xenografts acquire an artificial glycolytic*
517 *phenotype during in vitro cell culture*

518 A clear benefit of measuring ATP production rates is the ability to extend beyond commonly
519 used OCR:ECAR ratios to directly quantify changes in the balance between oxidative phosphorylation
520 and glycolysis. To illustrate this, we analyzed tumor cells from patient-derived glioma xenografts
521 either immediately harvested and purified from mice (~3 hr. isolation) or matched cells propagated in
522 *in vitro* gliomaspheres (>1 week culture period). *In vivo* evidence suggests that the enhanced aerobic
523 glycolysis observed in some glioma cell culture models may be driven, in part, by artifacts of cell
524 selection or *in vitro* growth conditions (Marin-Valencia *et al*, 2012). To explore this, we again
525 confirmed that our measurements of lactate using H^+ efflux matched enzymatic measurements for
526 these patient-derived cultures (Fig. 4A). We then examined the information that can be gained from
527 ATP production rates as opposed to OCR:ECAR ratios. In five different cell lines, *in vitro* cultured
528 glioma cells showed a significantly reduced OCR:ECAR ratio compared to matched cells assayed
529 immediately after purification from corresponding murine xenografts (*ex vivo*), indicating a relative
530 shift towards glycolysis in *in vitro* cultured cells (Figs. 4B).
531 Quantifying ATP production rates, however, extends this qualitative analysis. Glioma cells
532 analyzed *ex vivo* just after isolation and purification are highly dependent on oxidative phosphorylation
533 (~70% of total ATP). When cultured *in vitro*, however, cells undergo a remarkable shift in metabolism,
534 increasing their energy demand and switching to glycolysis as the dominant ATP-generating pathway
535 (Figs. 4C). Importantly, there is only a slight, statistically insignificant trend towards increased
536 oxidative phosphorylation, suggesting a specific reprogramming of glycolysis acquired upon *in vitro*
537 culture and not simply an increased energy demand met by both pathways. The result shows that
538 calculating ATP production from oxidative phosphorylation and glycolysis yields insights absent in
539 qualitative, ratio-based analyses, and further supports an *in vivo* bioenergetic role of mitochondria in
540 glioblastoma (Maher *et al*, 2012; Mashimo *et al*, 2014).
541 *ATP production rates demonstrate oxidative phosphorylation and glycolysis are differentially*
542 *engaged upon pro-inflammatory macrophage activation*
543 We then applied our calculation to study pro-inflammatory macrophage activation, another
544 form of immune cell activation associated with substantial metabolic alterations. Upon classical, "type
545 I" activation [LPS (± interferon-γ)], murine BMDMs profoundly remodel energy metabolism away from
546 oxidative phosphorylation (Van den Bossche *et al*, 2016) (Fig. 5A). ATP production is shifted to
547 glycolysis and mitochondria are repurposed to generate signals that support the pro-inflammatory
548 response (Mills *et al*, 2016; West *et al*, 2011; Lampropoulou *et al*, 2016). By measuring this switch
549 with a qualitative OCR:ECAR ratio, metabolic reprogramming with LPS was indistinguishable from
550 respiratory chain inhibition with complex I inhibitor rotenone (Fig. 5B, inset). However, quantifying
551 ATP production rates per cell revealed an increased energy demand associated with LPS activation,
552 discriminating between mitochondrial dysfunction and mitochondrial repurposing during macrophage
553 activation (Fig. 5B; Fig. EV5).

554 Quantifying ATP production rates over a range of LPS concentrations further highlights the
555 depth of information gained from the measurements. Qualitative OCR:ECAR ratios in response to
556 increasing LPS concentrations (1-30 ng/mL) suggest a uniform, coordinated shift away from oxidative
557 phosphorylation towards glycolysis to meet ATP demands upon activation (Fig. 5C, inset). Cellular
558 ATP production rates, on the other hand, surprisingly reveal these two pathways are engaged
559 independently. Increases in glycolysis and overall ATP utilization are observed with treatments as
560 low as 1 ng/mL LPS, whereas rates of mitochondrial ATP production are not compromised until LPS
561 concentrations rise above 10 ng/mL (Fig. 5C). Additionally, rates of maximal respiration are not
562 compromised at low concentrations of LPS that substantially increase glycolysis, further
563 demonstrating that the increase in glycolytic ATP is not simply a response to impaired mitochondrial
564 oxidative metabolism (Fig. 5D).
565 Indeed, the time-dependence of energetic activation further reveals that regulation of
566 mitochondrial and glycolytic ATP production are disengaged: glycolysis increases within two hours of
567 activation while rates of oxidative phosphorylation and maximal respiration are maintained up to at
568 least four hours (Figs. 5E&F). The results show the hallmark metabolic changes upon pro-
569 inflammatory macrophage activation are a composite phenotype where increases in ATP demand
570 and glycolysis are controlled distinctly from reductions in oxidative phosphorylation.
571
572 *ATP production rates can measure healthy bioenergetic changes during cell activation that are lost*
573 *with static ATP measurements*
574 We finally applied this analysis to models of acute cell activation to highlight the differences
575 between ATP production rates and measurements of ATP content. Healthy cell activation such as
576 neuronal plasma membrane depolarization or T cell receptor activation should minimally affect
577 snapshot-in-time intracellular ATP levels, as cells will readily adapt to a new steady-state of increased
578 ATP turnover (Brand & Nicholls, 2011). In primary cortical neurons, for example, addition of the Na^+-
579 channel activator veratridine stimulates Na^+/K^+-ATPase activity (Fig. 6A, top). Both oxygen
580 consumption and extracellular acidification rates increased in response to acute veratridine addition
581 (Choi *et al*, 2009) (Fig. 6A, bottom). Quantifying ATP production rates showed almost a three-fold
582 increase in the overall rate of ATP turnover upon depolarization, with the balance between oxidative
583 phosphorylation and glycolysis broadly unchanged upon activation (Fig. 6B). To demonstrate the
584 sensitivity of the assay, we used a sub-saturating amount of the Na^+/K^+-ATPase inhibitor ouabain (2
585 nM) to demonstrate the assay can pick up small but meaningful changes in the cellular ATP demand.
586 Substantial change in steady-state ATP utilization, however, did not appreciably change static ATP
587 levels, though levels were predictably altered in response to metabolic inhibitors coupled with
588 neuronal depolarization (Fig. 6C).

589 To further demonstrate the principle that ATP production rates provide information during cell
590 activation lost with steady-state measurements, we measured human $CD4^+$ T cell activation in
591 response to anti-CD3/CD28 stimulation. Here again, acute cell activation increased rates of both OCR
592 and ECAR (Fig. 6D). As is well documented, T cell activation caused a pronounced increase in
593 glycolysis to meet the energetic and biosynthetic demands of proliferation, cytokine production, and
594 clonal expansion (Maciver *et al*, 2013; Buck *et al*, 2017). Nonetheless, despite a four-fold increase in
595 glycolytic ATP production, comparing both pathways showed oxidative phosphorylation remained the
596 primary source of cellular ATP production, reinforcing an important role for mitochondria during early
597 T cell activation (Sena *et al*, 2013) (Fig. 6E). As was demonstrated previously for neurons, a
598 physiological increase in the ATP demand that is readily met by T cells did not manifest in
599 substantially altered ATP levels (Fig. 6F). In total, the results show real-time ATP production rates
600 can reveal activation-associated changes in energy metabolism that static ATP levels cannot.
601
602 **DISCUSSION**
603
604 *ATP fluxes during cell activation*
605 Our empirical approach to adjust proton efflux rates for respiratory acidification enables
606 quantification of lactate efflux using OCR and ECAR. Furthermore, obtaining quantitative lactate
607 readouts from the XF Analyzer allows estimation of cellular ATP production rates. ATP production
608 rates from both oxidative phosphorylation and glycolysis provide additional insight into how ATP
609 utilization is distributed during cell adaptation and activation. For example, *in vivo* stable isotope
610 tracing has shown that *in vitro* models of glioblastoma and other cancers can overestimate the
611 contribution of glycolysis to energy metabolism (Faubert *et al*, 2017; Marin-Valencia *et al*, 2012;
612 Momcilovic *et al*, 2019). In support of this, matched samples of patient-derived glioblastoma cells
613 clearly show the acquisition of an artificially high ATP demand driven almost entirely by a five-fold
614 increase in glycolysis in cells cultured *in vitro* relative to those assayed immediately after isolation
615 from murine orthotopic xenografts.
616 Additionally, the assay reveals that cells can adjust the balance of ATP production differently
617 depending on the type of activation and biological context. As an example, acute activation of the
618 Na^+/K^+-ATPase in primary cortical neurons substantially increases the ATP demand in a way that
619 does not broadly change the proportion of ATP produced by oxidative phosphorylation and glycolysis.
620 Despite an acute, 2.5-fold increase in ATP production, the balance between the two pathways
621 remained roughly constant with about 85% of the total ATP produced by mitochondria. It is sometimes
622 stated that the Na^+/K^+-ATPase and other plasma membrane ATPases preferentially rely on ATP
623 produced by glycolysis (Epstein *et al*, 2014; Sepp *et al*, 2014). However, our results do not support

624 this relationship, at least in two-dimensional cell culture models not subject to microenvironmental
625 gradients.
626 Unlike the instantaneous increase in ATP demand elicited by plasma membrane
627 depolarization, immune cell activation shows that cells can redistribute the balance between oxidative
628 phosphorylation and glycolysis when activating appropriate signaling cascades. Both T cell antigen
629 receptor (TCR)-linked activation in human T cells as well as TLR-mediated activation of murine
630 macrophages demonstrated that the increase in ATP utilization upon cell activation was increasingly
631 met by glycolysis relative to the naïve state. In T cells this increased glycolytic flux supports
632 generation of biosynthetic intermediates necessary for cell growth and expansion (Maciver *et al*,
633 2013). Given that many types of TLR activation cause growth arrest in murine macrophages, the
634 observed increase in glycolysis serves a different role. For example, the increase in glycolysis is likely
635 associated with increased flux through the pentose phosphate pathways to support cytoplasmic
636 NADPH production and fuel the anti-microbial NADPH oxidase (Cathcart, 2004). In fact, the approach
637 highlights that regulation of glycolysis and oxidative phosphorylation are disengaged during the pro-
638 inflammatory activation of macrophages. Rather than a coordinated process where mitochondrial
639 ATP production decreases alongside a matched increase in glycolysis, pro-inflammatory stimuli can
640 substantially increase glycolysis without changing rates of oxidative phosphorylation.
641
642 *Adjusting proton production rates to quantify lactate efflux*
643 In line with previous reports, our empirical approach determined that glycolytic and respiratory
644 acidification were the only dominant contributors to the extracellular acidification rate under normal
645 assay conditions. By and large, other reactions that could result in a net pH change of the medium
646 and alter the H^+ efflux rate either (i) did not have with fluxes comparable to those of respiratory and
647 glycolytic acidification, or (ii) occurred proportionally with respiratory CO_2 evolution or lactate efflux
648 (e.g. CO_2 evolution from the pentose phosphate pathway) and fell within a reasonable margin of
649 experimental error. Cell types or experimental conditions that may deviate from this framework are
650 addressed in the "Best practices" section of the Discussion.
651 Although we demonstrate that the H^+ efflux rate can quantitatively measure lactate efflux after
652 accounting for respiratory CO_2, the empirical values obtained did not follow the expected
653 stoichiometry for either lactate:H^+ or H^+:O_2 and were inconsistent with prior work (Mookerjee *et al*,
654 2015). These deviations from expected stoichiometry presented here, however, have theoretical and
655 experimental support. The value of 1.53 ± 0.12 for the lactate:H^+ can be explained in part by
656 incomplete coverage of the plate well by the fluorometric sensor in the XF cartridge, as cells in the
657 center of well have a far greater effect on the readings than those on the rim.
658 In fact, the expected lactate:H^+ value of ~1 is obtained when cells are only within the circle
659 connecting the three microplate risers, roughly corresponding to the XF96 fluorometric sensor area.

660 The demonstration that cells directly under the measurement sensor are preferentially, if not
661 exclusively, read by the cartridge suggests that there is no systematic error with the enzymatic lactate
662 measurements. Additionally, the result implies a 1:1 lactate:H^+ ratio should never have been
663 expected, particularly in older instruments where the fluorometric sensors consist of two small spots
664 (Gerencser *et al*, 2009) and not the larger smears found in newer instruments. Seahorse XF Wave
665 software now incorporates this correction into the Proton Efflux Rate (PER) parameter for all multi-
666 well platforms, accounting for the buffering power of the medium and incorporating the geometric
667 corrections obtained from this work.

668 The H^+:O_2 values from our analysis also deviate from theoretical stoichiometries expected
669 from the complete oxidation of known substrates. Nonetheless, the obtained values change with the
670 appropriate directionality and magnitude in response to oxidizing varying energy substrates in both
671 intact cells and isolated mitochondria. Moreover, lactate efflux rates calculated from the XF Analyzer
672 using an H^+:O_2 of 0.38 $\pm$ 0.05 to adjust for respiratory CO_2 matched enzymatic lactate assays,
673 suggesting there was no systemic error in measuring buffering power of the experimental medium.

674 Notably, the discrepancy between the obtained and expected H^+:O_2 values persists in isolated
675 mitochondria, where the experiments are highly controlled and the metabolic reactions are well
676 defined. In this system, the apparent H^+:O_2 values for a truncated reaction where mitochondria are
677 offered pyruvate and malate to generate citrate (theoretical H^+:O_2 = 1 (Mookerjee *et al*, 2015)) are
678 more than 3-fold lower than what is expected in principle and previously observed. The result is likely
679 due, in part, to the different ways the XF Wave software calculates rates of H^+ efflux and O_2
680 consumption. While the reported rates of H^+ production are a straightforward measurement, the
681 instrument reports rates of O_2 consumption only after an empirical correction to deconvolute the
682 effects of back-diffusion of ambient oxygen into the measurement microchamber(Gerencser *et al*,
683 2009). This includes use of an 'apparent chamber volume' that is 3-times greater than the actual
684 measurement chamber volume to account for oxygen storage in the walls of the polystyrene
685 microplate, and the algorithmic constants were determined by matching respiration rates obtained
686 from synaptoneurosomes in the XF Analyzer with values obtained from a platinum-based oxygen
687 electrode (Gerencser *et al*, 2009).

688 Crucially, these corrections would necessarily account, at least partially, for respiration in
689 material along the rim of the plate unseen by the measurement sensor because they are clamped to
690 values obtained from a Clark-type electrode. However, no such corrections for material unseen by
691 the measurement sensor are made for rates of medium acidification. As such, it is expected that rates
692 of H^+ production are consistently underestimated relative to rates of O_2 consumption, and that the
693 observed H^+:O_2 ratios fall below theoretical predictions. Put simply, while software corrections adjust
694 OCR to reflect the full well, this is not the case when measuring H^+ production.
695

696 *Assumptions and limitations in calculating ATP production rates*

697 Notwithstanding the deviation from expected values, the consensus values obtained for
698 lactate:H^+ and the H^+:O_2 accurately adjust for respiratory CO_2 and can be used to quantitatively reflect
699 lactate efflux. They can therefore be used to convert oxygen consumption rates and H^+ efflux rates
700 into estimates of ATP production as detailed in the Appendix Worksheet.

701 Any approach to estimate ATP production rate, be it the empirical approach presented here
702 or ones based on theoretical principles (Mookerjee *et al*, 2017), are subject to limitations and rely on
703 multiple assumptions. Our empirical approach uses an average H^+:O_2 value for use with standardized
704 experiment medium for cellular bioenergetics: DMEM supplemented with glucose, glutamine, and
705 pyruvate. This approach, however, precludes the ability to estimate ATP supply changes upon shifts
706 in cellular substrate preference (e.g. from fatty acids to glucose) in response to external cues. In
707 principle, this could be done by strictly defining the medium composition and applying different H^+:O_2
708 values based on assumptions or measurements of what substrates are being oxidized.

709 Additional limitations associated with our approach are (i) use of an approximate P:O value
710 and (ii) an underestimation of glycolytic ATP as described in the results. Both result from conducting
711 experiments in a composite medium more like culture conditions with multiple oxidizable substrates
712 available. It is therefore difficult to know, and perhaps unwise to assume, the fractional contribution
713 of individual substrates to the oxygen consumption rate.

714 We therefore chose to use an approximate P:O ratio and not to account for glycolytic ATP
715 produced during the complete oxidation of glucose. This approach did not significantly alter
716 measurements of glycolytic ATP in A549 lung adenocarcinoma cells, but the experimental conditions
717 substantially increased rates of oxidative phosphorylation and respiratory capacity. The pre-set
718 calculations of the Seahorse Analytical Software Tools follow this framework: they incorporate
719 average H^+:O_2 and lactate:H^+ values, use an approximate P:O ratio, and ignore the glycolytic ATP
720 contribution from complete glucose oxidation.

721

722 *Best practices for calculating of ATP production rates*

723 Many of the best practices associated with this particular assay are shared with Seahorse XF
724 assays in general. These include optimizing the plating density for suitable rates, ensuring all
725 measurements are conducted with rates at a relatively stable steady-states, using the inner 60 wells
726 of the XF96 microplate to avoid temperature and evaporative effects, and following best practices for
727 normalization (Divakaruni & Jastroch, 2022). Of course, any acute compound treatments should
728 precede the injection of rotenone and antimycin A.

729 When calculating the buffering power of the experimental medium, it is always best practice
730 to use a non-volatile acid (e.g. H_2SO_4) or two distinct calibrations (e.g. one with HCl and one with
731 H_2SO_4) to minimize instrument and operational error. The buffering power should be checked or

732 recalculated when critical parts of the measurement process are changed – such as switching
733 cartridge lot numbers, batches of medium, or instruments – but does not necessarily need to be
734 calculated alongside each experimental run. In the 96-well instrument, it is often convenient to use
735 columns 1 and 12 of the microplate for these calculations as is shown in the Appendix Worksheet.
736 Additionally, it may be that the approximations used for this method are substantively
737 inaccurate in specific cases depending on the experimental hypothesis and quantitative rigor
738 required. For example, rates of lactate efflux may be particularly low when using acutely isolated
739 primary cells, and therefore the non-zero background rate of H^+ efflux (Figs. 1E and 2C) may
740 represent a substantial component of the signal and skew results. Furthermore, conditions where the
741 rate of lactate efflux is matched by organic acid efflux of the same magnitude may also be less
742 amenable to using consensus values of lactate:H^+ and H^+:O_2. Indeed, this is apparent in
743 noradrenaline-stimulated adipocytes known to release fatty acids: our XF Analyzer calculations based
744 on H^+ release estimated an almost two-fold increase in lactate efflux, whereas the enzymatic assay
745 showed a 1.5-fold increase (Fig. EV4). Additionally, under extreme, non-physiological conditions such
746 as neurons depolarized in the absence of glucose, release of glutamate and other neurotransmitters
747 resulted in a profound increase in acidification entirely independent of lactate efflux.
748 As such, any system in which the investigator believes that non-lactate acid efflux could
749 prohibitively alter the conclusions should consider independently calculating lactate efflux with other
750 methods such as enzymology or mass spectrometry. However, the empirical approach presented
751 here provides the framework for researchers to calculate lactate:H^+ and H^+:O_2 values tailored to any
752 (monolayer) model system or experimental conditions.
753
754 **ACKNOWLEDGEMENTS**
755 A.S.D. is supported by National Institutes of Health (NIH) Grants R35GM138003, P30DK063491, and
756 P50CA092131, as well as the W.M. Keck Foundation. B.R.D. is supported by the U.S. Department
757 of Defense National Defense Science and Engineering (NDSEG) Fellowship Program. A.E.J. was
758 supported by the UCLA Tumor Cell Biology Training Program (T32 CA009056) and a Eugene V. Cota
759 Robles Scholarship. A.B.B. was supported by the UCLA Chemistry-Biology Interface Training Grant
760 (T32GM136614). S.J.B. is supported by NIH Grants P01HL146358 and R01HL157710.
761
762 **AUTHOR CONTRIBUTIONS**
763 A.S.D. and N.R. supervised all aspects of the project. A.S.D., N.R., S.J.B., A.N.M., B.P.D., D.A.N.,
764 A.N., D.A.F., C.A. and O.S. conceptualized the study and/or designed the research plan. A.S.D.,
765 B.R.D., K.K.O., A.B.B., W.Y.H., A.E.J., P.S., D.M., A.J.B., L.S., G.W.R., and N.R. conducted
766 experiments. A.S.D., B.R.D., K.K.O., A.B.B., W.Y.H., A.E.J., P.S., and N.R. analyzed the data. A.S.D.,

767 B.R.D., and N.R. prepared the figures and wrote the manuscript with editing and approval from all
768 authors.
769
770 **DISCLOSURES**
771 N.R., G.W.R., P.S., and A.N. are currently employees and shareholders of Agilent Technologies.
772 B.P.D., and D.A.F. were previously employees and shareholders of Agilent Technologies at the time
773 of this study. A.S.D. has previously served as a paid consultant for Agilent Technologies.
774

775 **FIGURE LEGENDS**

776 **Figure 1 – Extracellular acidification is directly proportional to lactate efflux in the absence of**
777 **respiration**

778 All data are mean ± S.E.M. unless otherwise specified.

779 (A) Sample trace of H_2SO_4 injections to determine buffer capacity of Seahorse experimental medium.
780 Error bars are obscured by the symbol. (n=16 technical replicates from a single experiment)

781 (B) Changes in pH from sequential additions of 62.5 nmol H^+ via the injector ports. The experimental
782 medium is DMEM supplemented with 8 mM glucose, 2 mM glutamine, 2 mM pyruvate, and the
783 indicated concentration of HEPES (pH 7.4). The microchamber volume of the 96-well XF Analyzer
784 is 2.28 μL. Step-by-step calculations are available in the Appendix Worksheet. (n=6 experimental
785 replicates)

786 (C) The H^+ production rate is given for A549 cells treated acutely (20 minutes prior to assay) with
787 varying concentrations of 2-deoxyglucose (2DG) or 2DG with iodoacetic acid (IAA) to block
788 glycogenolysis. The experimental medium contains 5 mM glucose with 5 mM HEPES, 200 nM
789 rotenone (complex I inhibitor), 1 μM antimycin (complex III inhibitor), and 2 μM oligomycin
790 (complex V inhibitor to block 'reverse' hydrolysis of ATP upon respiratory chain inhibition). (n=6
791 biological replicates)

792 (D) Sample trace of standard curve used to measure lactate collected from experimental medium.
793 (n=3 technical replicates)

794 (E) Plot of lactate efflux rates measured as in (D) against H^+ production rates measured in the
795 Seahorse XF Analyzer. Experimental conditions and titration of the rate with glycolytic inhibitors
796 are as in (C). Parenthetical values given in the key are the fitted slopes for each individual cell
797 type. (n=6 biological replicates)

798 (F) Aggregate lactate:H^+ ratios, calculated as in (E) for 17 different cell types, yielding an average
799 value of 1.53 ± 0.12 (mean ± standard deviation).

800

801 **Figure 2 – Extracellular acidification is directly proportional to respiration in the absence of**
802 **glycolysis**

803 All data are mean ± S.E.M. unless otherwise specified.

804 (A) Sample kinetic trace of oxygen consumption in HepG2 cells in medium containing 5 mM pyruvate,
805 5 mM glutamine, 5 mM HEPES, 2 mM 2-deoxyglucose, and 50 μM iodoacetate. Where indicated,
806 the respiratory rate was modulated with addition of UK5099 (MPC inhibitor to block pyruvate
807 oxidation) and BPTES (glutaminase inhibitor to block glutamine oxidation). (n=8 technical
808 replicates from a single experiment)

809 (B) Sample kinetic trace of H^+ production rates measured from (A). (n=8 technical replicates from a
810 single experiment)
811 (C) Plot of H^+ production rates against oxygen consumption rates for experiments conducted as in (A
812 & B). The rates are titrated with mitochondrial effectors (oligomycin, varying concentrations of
813 FCCP, rotenone/antimycin A) or combined treatment with UK5099 and BPTES. Individual points
814 are taken as the average values for all measurements for a particular treatment (e.g. average of
815 three measurements in response to initial FCCP addition). Parenthetical values given in the key
816 are the fitted slopes for each individual cell type. (n=6 biological replicates)
817 (D) Aggregate H^+:O_2 ratios, calculated as in (C) for 21 different cell types, yielding an average value
818 of 0.38 ± 0.05 (mean ± standard deviation).
819
820 **Figure 3 – Transformation of ECAR into lactate efflux allows calculation of ATP production**
821 **rates**
822 All data are mean ± S.E.M. unless otherwise specified.
823 (A) The H^+ production rate from the XF Analyzer (left bar in each graph), the calculated lactate efflux
824 rate from the XF Analyzer (center bar), and the lactate efflux rate measured from an enzymatic
825 assay (right bar) are given for A549 cells, C2C12 cells, and primary bone marrow-derived
826 macrophages (BMDMs). Cells are offered 8 mM glucose, 2 mM pyruvate, and 2mM glutamine in
827 experimental medium supplemented with 5 mM HEPES. The shaded component of the H^+
828 production rates for each cell type is the calculated contribution from respiratory acidification. (n≥4
829 biological replicates)
830 (B) The oxygen consumption rate from a representative experiment with A549 cells is presented.
831 Assay medium is as in (A). The parameters needed to calculate the ATP production rate are
832 indicated with in the figure. (n=6 technical replicates)
833 (C) The H^+ production rate from the kinetic trace in (B) is presented. Only the initial rates are shown,
834 as these are the only measurements required to calculate the ATP production rate. (n=6 technical
835 replicates)
836 (D) ATP production rates calculated for A549 cells in DMEM supplemented with 8 mM glucose, 2 mM
837 glutamine, and 2 mM pyruvate and Krebs-Henseleit buffer supplemented with only 10 mM
838 glucose. (n=4 biological replicates)
839 (E) Maximal respiratory rates measured in response to oligomycin and FCCP for treatments as in
840 (D). (n=4 biological replicates)
841
842 **Figure 4 – ATP production rates capture changes OCR:ECAR ratios cannot in primary cancer**
843 **cell models**
844 All data are mean ± S.E.M. unless otherwise specified. *, $p<0.05$; **, $p<0.01$.

845 (A) Lactate as measured by the XF Analyzer matches enzymatic lactate measurements for a panel
846 of patient-derived, gliomasphere (GS) cell lines after *in vitro* culture. (n≥3 biological replicates for
847 each line)
848 (B) OCR:ECAR ratios for patient-derived glioblastoma cells cultured *in vitro* or assayed immediately
849 after harvesting from mouse xenographs (*ex vivo*). Cell lined used were GS25, GBM39, GS114,
850 GS116, GS122.
851 (C) ATP Production rates from cell types as in (B).
852
853 **Figure 5 – ATP production rates highlight independent regulation of glycolysis and oxidative**
854 **phosphorylation during LPS activation of macrophages**
855 All data are mean ± S.E.M. unless otherwise specified. *, p<0.05; **, p<0.01; ***, p<0.001.
856 (A) The oxygen consumption rate and H^+ production rate from a representative experiment with
857 BMDMs in response to treatment with 50 ng/mL LPS for 24 hr. (n=5 technical replicates)
858 (B) The ATP production rate is calculated for BMDMs in response to 50 ng/mL LPS or 50 nM rotenone
859 for 24 hr. (*Inset*) The OCR:ECAR ratio is presented for each condition. (n=6 biological replicates)
860 Representative images used for cell counts are provided in the supplementary material.
861 (C) The ATP production rate is calculated for BMDMs in response to varying concentrations of LPS
862 ranging from 1-30 ng/mL for 24 hr. (*Inset*) The OCR:ECAR ratio is presented for each condition.
863 (n=5 biological replicates)
864 (D) FCCP-stimulated, maximal respiratory rates from treatments as in (C). (n=5 biological replicates)
865 (E) The ATP production rate is calculated for BMDMs in response to treatment for 2 or 4 hr. with 50
866 ng/mL LPS. (*Inset*) The OCR:ECAR ratio is presented for each condition. (n=4 biological
867 replicates)
868 (F) FCCP-stimulated, maximal respiratory rates from treatments as in (E). (n=4 biological replicates)
869
870 **Figure 6 – ATP production rates capture healthy changes in cell activation that static ATP**
871 **measurements cannot**
872 All data are mean ± S.E.M. unless otherwise specified. *, p<0.05; **, p<0.01; ***, p<0.001.
873 (A) (*Top*) Schematic depicting increase in Na^+/K^+-ATPase activity by veratridine, which will depolarize
874 the plasma membrane by increasing sodium influx, thereby triggering ouabain-sensitive increases
875 in ATP production. (*Bottom*) Sample kinetic traces of OCR and ECAR in primary neurons upon
876 acute addition of 1.5 μM veratridine. (n=10 technical replicates)
877 (B) ATP production rates from oxidative phosphorylation ($ATP_{Ox.Phos.}$, blue) and glycolysis ($ATP_{Glyco.}$,
878 red) in response to (*left to right*) vehicle, 1.5 μM veratridine, veratridine plus 2 nM ouabain to
879 demonstrate sensitivity of the assay, and veratridine plus 1 μM antimycin, 5 mM 2-deoxyglucose,

880 and 1 mM iodoacetic acid to cause an energy crisis and deplete ATP levels. (n=4 biological
881 replicates)
882 (C) Total ATP levels measured by luminescence after 15 min treatments as in (B). (n=4 biological
883 replicates)
884 (D) Sample kinetic traces of OCR and ECAR in murine T cells acutely activated with anti-CD3/CD28.
885 (n=4 technical replicates)
886 (E) ATP production rates from oxidative phosphorylation and glycolysis in response to anti-
887 CD3/CD28. (n=3 biological replicates)
888 (F) Total ATP levels measured by luminescence after 30 min activation as in (E). (n=3 biological
889 replicates)
890
891

892 **REFERENCES**

893 Affourtit C & Brand MD (2009) Measuring mitochondrial bioenergetics in INS-1E insulinoma cells.
894 *Methods Enzymol* 457: 405–424
895 Van den Bossche J, Baardman J, Otto NA, van der Velden S, Neele AE, van den Berg SM, Luque-
896 Martin R, Chen HJ, Boshuizen MCS, Ahmed M, *et al* (2016) Mitochondrial Dysfunction Prevents
897 Repolarization of Inflammatory Macrophages. *Cell Rep*
898 Van den Bossche J, O'Neill LA & Menon D (2017) Macrophage Immunometabolism: Where Are We
899 (Going)? *Trends Immunol* doi:10.1016/j.it.2017.03.001 [PREPRINT]
900 Brand MD (2005) The efficiency and plasticity of mitochondrial energy transduction. *Biochem Soc*
901 *Trans* 33: 897–904
902 Brand MD & Nicholls DG (2011) Assessing mitochondrial dysfunction in cells. *Biochemical Journal*
903 doi:10.1042/BJ20110162 [PREPRINT]
904 Buck MD, Sowell RT, Kaech SM & Pearce EL (2017) Metabolic Instruction of Immunity. *Cell*
905 doi:10.1016/j.cell.2017.04.004 [PREPRINT]
906 Cathcart MK (2004) Regulation of Superoxide Anion Production by NADPH Oxidase in
907 Monocytes/Macrophages: Contributions to Atherosclerosis. *Arterioscler Thromb Vasc Biol*
908 doi:10.1161/01.ATV.0000097769.47306.12 [PREPRINT]
909 Chandel NS (2015) Navigating metabolism Cold Spring Harbor Laboratory Press
910 Chen C-T, Shih Y-R V., Kuo TK, Lee OK & Wei Y-H (2008) Coordinated changes of mitochondrial
911 biogenesis and antioxidant enzymes during osteogenic differentiation of human mesenchymal
912 stem cells. *Stem Cells* 26: 960–968
913 Choi SW, Gerencser AA & Nicholls DG (2009) Bioenergetic analysis of isolated cerebrocortical nerve
914 terminals on a microgram scale: Spare respiratory capacity and stochastic mitochondrial failure.
915 *J Neurochem*
916 DeBerardinis RJ & Chandel NS (2020) We need to talk about the Warburg effect. *Nat Metab* 2: 127–
917 129
918 Divakaruni AS & Jastroch M (2022) A practical guide for the analysis, standardization and
919 interpretation of oxygen consumption measurements. *Nat Metab* 4: 978–994
920 Divakaruni AS, Paradyse A, Ferrick DA, Murphy AN & Jastroch M (2014) Analysis and interpretation
921 of microplate-based oxygen consumption and pH data. In *Methods in Enzymology*
922 Divakaruni AS, Wallace M, Buren C, Martyniuk K, Andreyev AY, Li E, Fields JA, Cordes T, Reynolds
923 IJ, Bloodgood BL, *et al* (2017) Inhibition of the mitochondrial pyruvate carrier protects from
924 excitotoxic neuronal death. *Journal of Cell Biology*
925 Ducker GS & Rabinowitz JD (2017) One-Carbon Metabolism in Health and Disease. *Cell Metab* 25:
926 27
927 Epstein T, Xu L, Gillies RJ & Gatenby RA (2014) Separation of metabolic supply and demand: aerobic
928 glycolysis as a normal physiological response to fluctuating energetic demands in the
929 membrane. *Cancer Metab* 2
930 Faubert B, Li KY, Cai L, Hensley CT, Kim J, Zacharias LG, Yang C, Do QN, Doucette S, Burguete D,
931 *et al* (2017) Lactate Metabolism in Human Lung Tumors. *Cell* 171: 358-371.e9
932 Gerencser AA, Neilson A, Choi SW, Edman U, Yadava N, Oh RJ, Ferrick DA, Nicholls DG & Brand
933 MD (2009) Quantitative microplate-based respirometry with correction for oxygen diffusion. *Anal*
934 *Chem*
935 Gillies RJ, Robey I & Gatenby RA (2008) Causes and consequences of increased glucose
936 metabolism of cancers. *J Nucl Med* 49 Suppl 2
937 Gosa L, Ta L & Nathanson DA (2019) Processing of Primary Patient Tumors and Subsequent
938 Generation of Primary Cell Lines. *Methods Mol Biol* 1897: 425–431
939 Gu W, Gaeta X, Sahakyan A, Chan AB, Hong CS, Kim R, Braas D, Plath K, Lowry WE & Christofk
940 HR (2016) Glycolytic Metabolism Plays a Functional Role in Regulating Human Pluripotent Stem
941 Cell State. *Cell Stem Cell* 19: 476–490
942 Gubser PM, Bantug GR, Razik L, Fischer M, Dimeloe S, Hoenger G, Durovic B, Jauch A & Hess C
943 (2013) Rapid effector function of memory CD8+ T cells requires an immediate-early glycolytic
944 switch. *Nat Immunol* 14: 1064–1072

Hazim RA, Paniagua AE, Tang L, Yang K, Kim KKO, Stiles L, Divakaruni AS & Williams DS (2022) Vitamin B3, nicotinamide, enhances mitochondrial metabolism to promote differentiation of the retinal pigment epithelium. *J Biol Chem* 298

Hong CS, Graham NA, Gu W, Espindola Camacho C, Mah V, Maresh EL, Alavi M, Bagryanova L, Krotee PAL, Gardner BK, *et al* (2016) MCT1 Modulates Cancer Cell Pyruvate Export and Growth of Tumors that Co-express MCT1 and MCT4. *Cell Rep* 14: 1590–1601

Hsieh WY, Williams KJ, Su B & Bensinger SJ (2020) Profiling of mouse macrophage lipidome using direct infusion shotgun mass spectrometry. *STAR Protoc* 2

Kim HJ & Magrané J (2011) Isolation and culture of neurons and astrocytes from the mouse brain cortex. *Methods Mol Biol* 793: 63–75

Koveal D, Díaz-García CM & Yellen G (2020) Fluorescent Biosensors for Neuronal Metabolism and the Challenges of Quantitation. *Curr Opin Neurobiol* 63: 111–121

Kubli DA, Zhang X, Lee Y, Hanna RA, Quinsay MN, Nguyen CK, Jimenez R, Petrosyans S, Murphy AN & Gustafsson ÅB (2013) Parkin protein deficiency exacerbates cardiac injury and reduces survival following myocardial infarction. *J Biol Chem* 288: 915–926

Kushnareva YE, Wiley SE, Ward MW, Andreyev AY & Murphy AN (2005) Excitotoxic injury to mitochondria isolated from cultured neurons. *Journal of Biological Chemistry* 280: 28894–28902

Lampropoulou V, Sergushichev A, Bambouskova M, Nair S, Vincent EE, Loginicheva E, Cervantes-Barragan L, Ma X, Huang SCC, Griss T, *et al* (2016) Itaconate Links Inhibition of Succinate Dehydrogenase with Macrophage Metabolic Remodeling and Regulation of Inflammation. *Cell Metab*

Lewis CA, Parker SJ, Fiske BP, McCloskey D, Gui DY, Green CR, Vokes NI, Feist AM, Vander Heiden MG & Metallo CM (2014) Tracing compartmentalized NADPH metabolism in the cytosol and mitochondria of mammalian cells. *Mol Cell* 55: 253–263

Lundholt BK, Scudder KM & Pagliaro L (2003) A simple technique for reducing edge effect in cell-based assays. *J Biomol Screen* 8: 566–570

Lunt SY & Vander Heiden MG (2011) Aerobic glycolysis: meeting the metabolic requirements of cell proliferation. *Annu Rev Cell Dev Biol* 27: 441–464

Maciver NJ, Michalek RD & Rathmell JC (2013) Metabolic Regulation of T Lymphocytes. *http://dx.doi.org/101146/annurev-immunol-032712-095956* 31: 259–283

Maher EA, Marin-Valencia I, Bachoo RM, Mashimo T, Raisanen J, Hatanpaa KJ, Jindal A, Jeffrey FM, Choi C, Madden C, *et al* (2012) Metabolism of [U-13 C]glucose in human brain tumors in vivo. *NMR Biomed* 25: 1234–1244

Marin-Valencia I, Yang C, Mashimo T, Cho S, Baek H, Yang XL, Rajagopalan KN, Maddie M, Vemireddy V, Zhao Z, *et al* (2012) Analysis of Tumor Metabolism Reveals Mitochondrial Glucose Oxidation in Genetically Diverse Human Glioblastomas in the Mouse Brain In Vivo. *Cell Metab* 15: 827–837

Mashimo T, Pichumani K, Vemireddy V, Hatanpaa KJ, Singh DK, Sirasanagandla S, Nannepaga S, Piccirillo SG, Kovacs Z, Foong C, *et al* (2014) Acetate is a bioenergetic substrate for human glioblastoma and brain metastases. *Cell* 159: 1603–1614

McConnell HM, Owicki JC, Parce JW, Miller DL, Baxter GT, Wada HG & Pitchford S (1992) The cytosensor microphysiometer: biological applications of silicon technology. *Science* 257: 1906–1912

Mills EL, Kelly B, Logan A, Costa ASH, Varma M, Bryant CE, Tourlomousis P, Däbritz JHM, Gottlieb E, Latorre I, *et al* (2016) Succinate Dehydrogenase Supports Metabolic Repurposing of Mitochondria to Drive Inflammatory Macrophages. *Cell*

Momcilovic M, Jones A, Bailey ST, Waldmann CM, Li R, Lee JT, Abdelhady G, Gomez A, Holloway T, Schmid E, *et al* (2019) In vivo imaging of mitochondrial membrane potential in non-small-cell lung cancer. *Nature*

Mookerjee SA, Gerencser AA, Nicholls DG & Brand MD (2017) Quantifying intracellular rates of glycolytic and oxidative ATP production and consumption using extracellular flux measurements. *Journal of Biological Chemistry*

Mookerjee SA, Goncalves RLS, Gerencser AA, Nicholls DG & Brand MD (2015) The contributions of respiration and glycolysis to extracellular acid production. *Biochim Biophys Acta* 1847: 171–181

Moyes CD, Mathieu-Costello OA, Tsuchiya N, Filburn C & Hansford RG (1997) Mitochondrial biogenesis during cellular differentiation. *https://doi.org/101152/ajpcell19972724C1345* 272

Newell K, Franchi A, Pouyssegur J & Tannock I (1993) Studies with glycolysis-deficient cells suggest that production of lactic acid is not the only cause of tumor acidity. *Proc Natl Acad Sci U S A* 90: 1127–1131

Nicholls DG & Ferguson SJ (2013) Bioenergetics 4

Panic V, Pearson S, Banks J, Tippetts TS, Velasco-Silva JN, Lee S, Simcox J, Geoghegan G, Bensard C, Ry T van, *et al* (2020) Mitochondrial pyruvate carrier is required for optimal brown fat thermogenesis. *Elife* 9: 1–27

Pavlova NN & Thompson CB (2016) The Emerging Hallmarks of Cancer Metabolism. *Cell Metab* 23: 27–47

Pelletier M, Billingham LK, Ramaswamy M & Siegel RM (2014) Extracellular flux analysis to monitor glycolytic rates and mitochondrial oxygen consumption. In *Methods in Enzymology*

Rich PR & Maréchal A (2010) The mitochondrial respiratory chain. *Essays Biochem*

Rubio M, Avitabile D, Fischer K, Emmanuel G, Gude N, Miyamoto S, Mishra S, Schaefer EM, Brown JH & Sussman MA (2009) Cardioprotective stimuli mediate phosphoinositide 3-kinase and phosphoinositide dependent kinase 1 nuclear accumulation in cardiomyocytes. *J Mol Cell Cardiol* 47: 96–103

Sena LA, Li S, Jairaman A, Prakriya M, Ezponda T, Hildeman DA, Wang CR, Schumacker PT, Licht JD, Perlman H, *et al* (2013) Mitochondria are required for antigen-specific T cell activation through reactive oxygen species signaling. *Immunity* 38: 225–236

Sepp M, Sokolova N, Jugai S, Mandel M, Peterson P & Vendelin M (2014) Tight coupling of Na+/K+-ATPase with glycolysis demonstrated in permeabilized rat cardiomyocytes. *PLoS One* 9

Shin B, Benavides GA, Geng J, Koralov SB, Hu H, Darley-Usmar VM & Harrington LE (2020) Mitochondrial Oxidative Phosphorylation Regulates the Fate Decision between Pathogenic Th17 and Regulatory T Cells. *Cell Rep* 30: 1898-1909.e4

Sullivan WJ, Mullen PJ, Schmid EW, Flores A, Momcilovic M, Sharpley MS, Jelinek D, Whiteley AE, Maxwell MB, Wilde BR, *et al* (2018) Extracellular Matrix Remodeling Regulates Glucose Metabolism through TXNIP Destabilization. *Cell* 175: 117-132.e21

Tantama M & Yellen G (2014) Imaging changes in the cytosolic ATP-to-ADP ratio. *Methods Enzymol* 547: 355–371

Thompson BR, Lobo S & Bernlohr DA (2010) FATTY ACID FLUX IN ADIPOCYTES; THE IN'S AND OUT'S OF FAT CELL LIPID TRAFFICKING. *Mol Cell Endocrinol* 318: 24

Watt IN, Montgomery MG, Runswick MJ, Leslie AGW & Walker JE (2010) Bioenergetic cost of making an adenosine triphosphate molecule in animal mitochondria. *Proc Natl Acad Sci U S A* 107: 16823–16827

West AP, Brodsky IE, Rahner C, Woo DK, Erdjument-Bromage H, Tempst P, Walsh MC, Choi Y, Shadel GS & Ghosh S (2011) TLR signalling augments macrophage bactericidal activity through mitochondrial ROS. *Nature*

Wilson-Fritch L, Burkart A, Bell G, Mendelson K, Leszyk J, Nicoloro S, Czech M & Corvera S (2003) Mitochondrial biogenesis and remodeling during adipogenesis and in response to the insulin sensitizer rosiglitazone. *Mol Cell Biol* 23: 1085–1094

Zhao C, Wilson MC, Schuit F, Halestrap AP & Rutter GA (2001) Expression and distribution of lactate/monocarboxylate transporter isoforms in pancreatic islets and the exocrine pancreas. *Diabetes* 50: 361–366

Figure 1

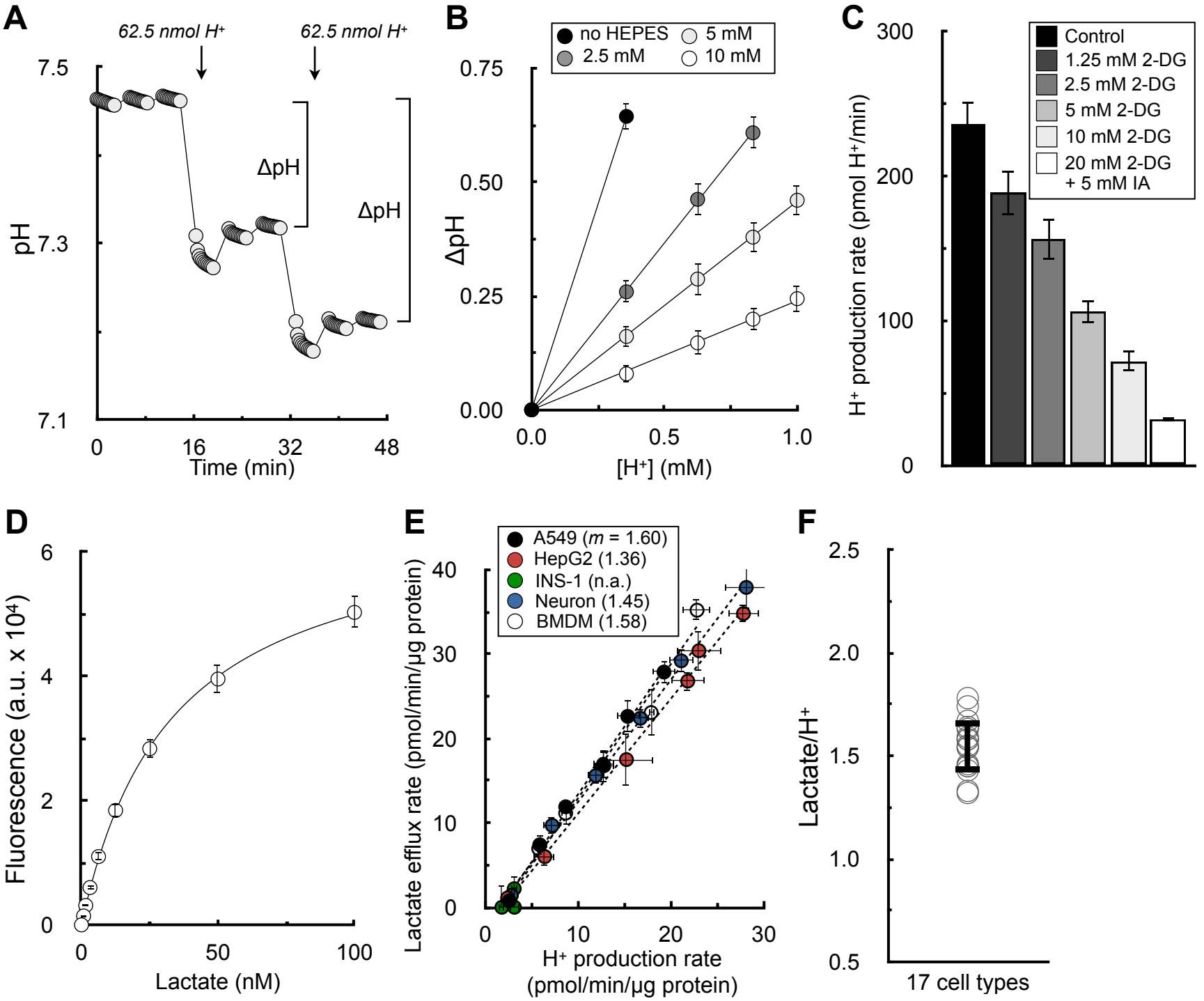
A
62.5 nmol H+
62.5 nmol H+
ΔpH
ΔpH
pH
7.5
7.3
7.1
0
16
32
48
Time (min)
B
no HEPES
2.5 mM
5 mM
10 mM
ΔpH
0.75
0.50
0.25
0.00
0.0
0.5
1.0
[H+] (mM)
C
Control
1.25 mM 2-DG
2.5 mM 2-DG
5 mM 2-DG
10 mM 2-DG
20 mM 2-DG
+ 5 mM IA
H+ production rate (pmol H+/min)
300
200
100
0
D
Fluorescence (a.u. x 10⁴)
6
4
2
0
0
50
100
Lactate (nM)
E
A549 (m = 1.60)
HepG2 (1.36)
INS-1 (n.a.)
Neuron (1.45)
BMDM (1.58)
Lactate efflux rate (pmol/min/µg protein)
40
30
20
10
0
0
10
20
30
H+ production rate
(pmol/min/µg protein)
F
Lactate/H+
2.5
2.0
1.5
1.0
0.5
17 cell types

Figure 2

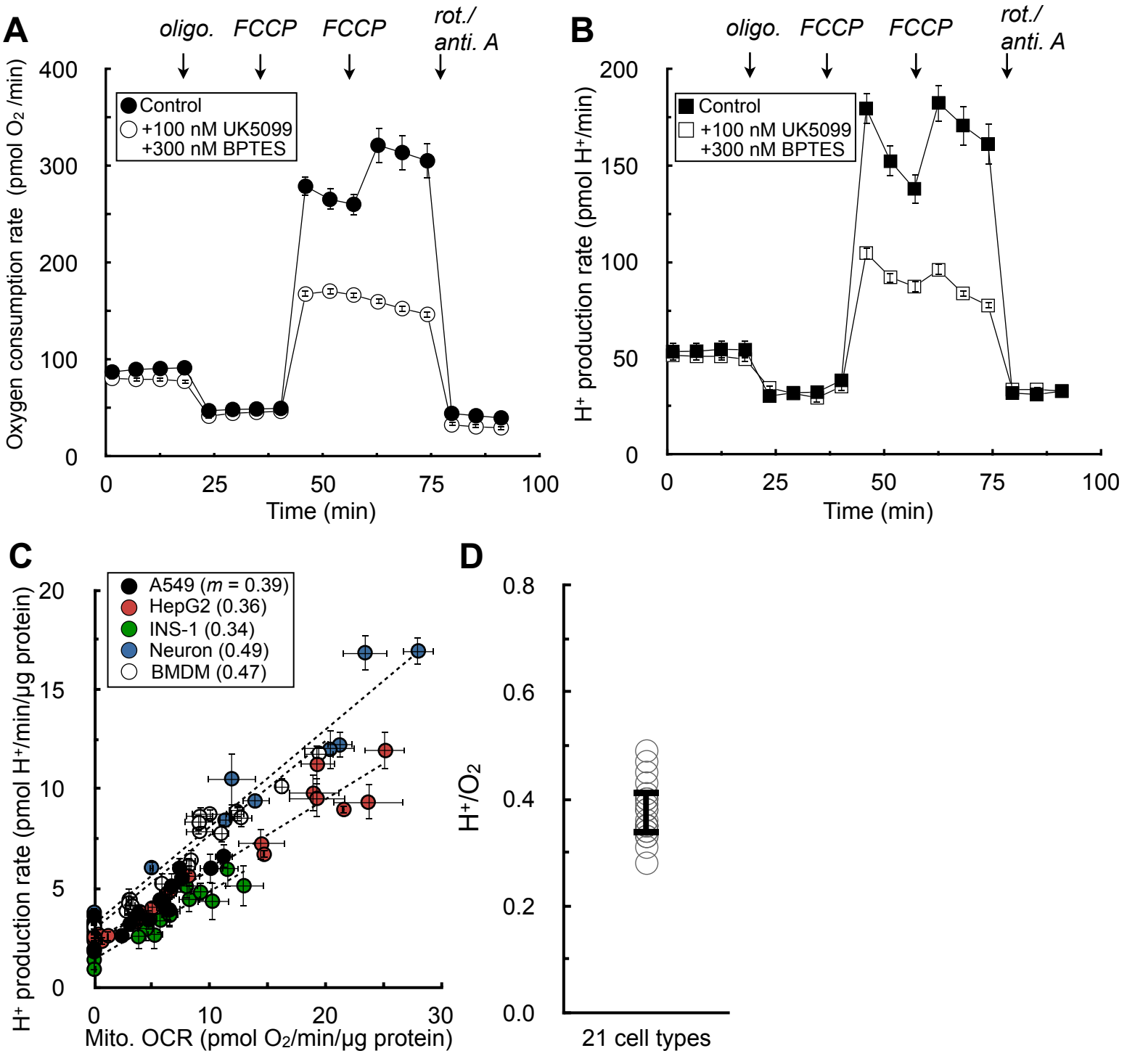
A
oligo.
FCCP
FCCP
rot./
anti. A
Control
+100 nM UK5099
+300 nM BPTES
Oxygen consumption rate (pmol O2 /min)
Time (min)
B
H+ production rate (pmol H+/min)
C
A549 (m = 0.39)
HepG2 (0.36)
INS-1 (0.34)
Neuron (0.49)
BMDM (0.47)
H+ production rate (pmol H+/min/µg protein)
Mito. OCR (pmol O2/min/µg protein)
D
H+/O2
21 cell types

Figure 3

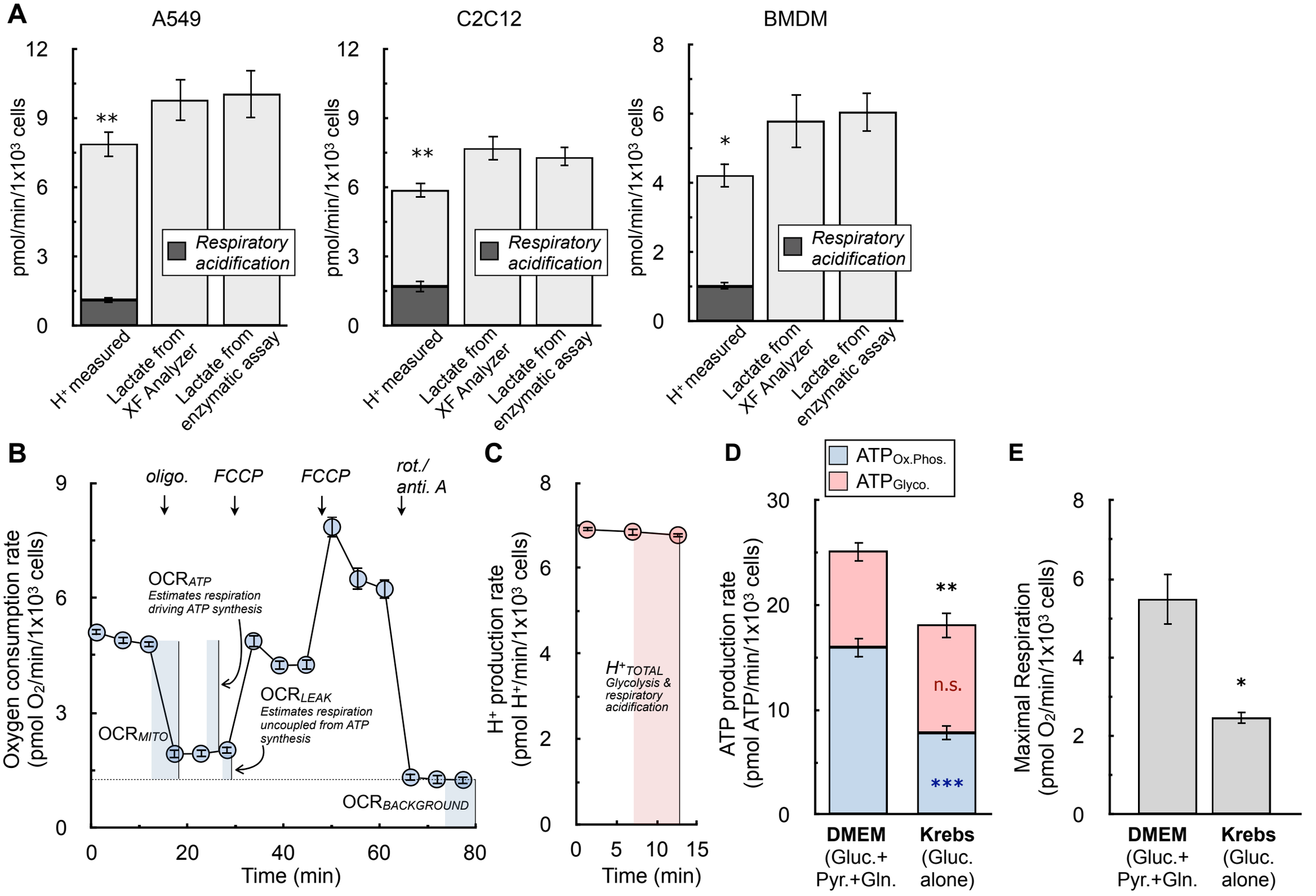
A
A549
C2C12
BMDM
pmol/min/1x10³ cells
Respiratory acidification
H⁺ measured
Lactate from XF Analyzer
Lactate from enzymatic assay
B
oligo.
FCCP
FCCP
rot./ anti. A
Oxygen consumption rate (pmol O₂/min/1x10³ cells)
OCR_ATP
Estimates respiration driving ATP synthesis
OCR_LEAK
Estimates respiration uncoupled from ATP synthesis
OCR_MITO
OCR_BACKGROUND
Time (min)
C
H⁺ production rate (pmol H⁺/min/1x10³ cells)
H⁺_TOTAL
Glycolysis & respiratory acidification
Time (min)
D
ATP_Ox.Phos.
ATP_Glyco.
ATP production rate (pmol ATP/min/1x10³ cells)
n.s.
DMEM (Gluc.+ Pyr.+Gln.)
Krebs (Gluc. alone)
E
Maximal Respiration (pmol O₂/min/1x10³ cells)
DMEM (Gluc.+ Pyr.+Gln.)
Krebs (Gluc. alone)

Figure 4

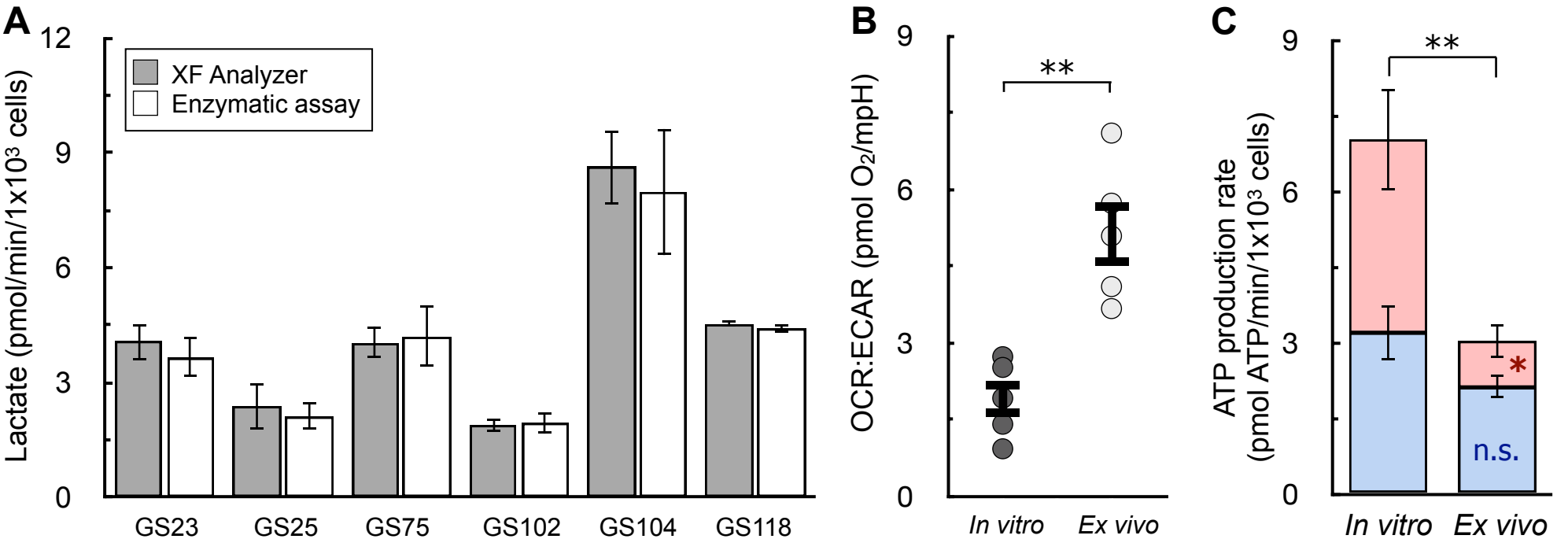
A
Lactate (pmol/min/1x10³ cells)
XF Analyzer
Enzymatic assay
0
3
6
9
12
GS23
GS25
GS75
GS102
GS104
GS118
B
OCR:ECAR (pmol O₂/mpH)
**
0
3
6
9
In vitro
Ex vivo
C
ATP production rate
(pmol ATP/min/1x10³ cells)
**
*
n.s.
0
3
6
9
In vitro
Ex vivo

Figure 5

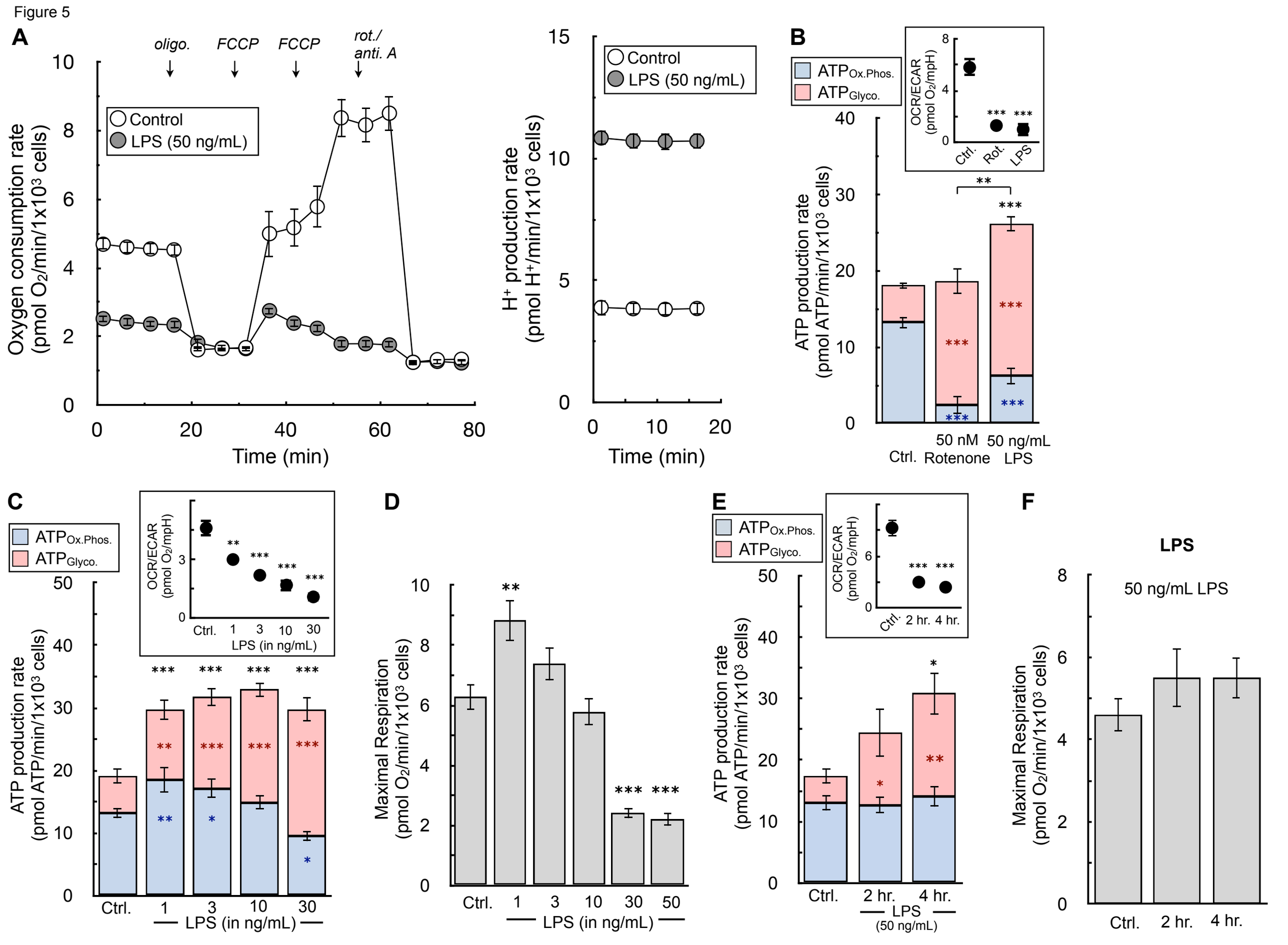
A
oligo.
FCCP
FCCP
rot./ anti. A
Control
LPS (50 ng/mL)
Oxygen consumption rate (pmol O2/min/1x10³ cells)
Time (min)
H+ production rate (pmol H+/min/1x10³ cells)
B
ATPOx.Phos.
ATPGlyco.
OCR/ECAR (pmol O2/mpH)
Ctrl.
Rot.
LPS
ATP production rate (pmol ATP/min/1x10³ cells)
50 nM Rotenone
50 ng/mL LPS
C
LPS (in ng/mL)
D
Maximal Respiration (pmol O2/min/1x10³ cells)
E
2 hr.
4 hr.
F
LPS
50 ng/mL LPS

Figure 6

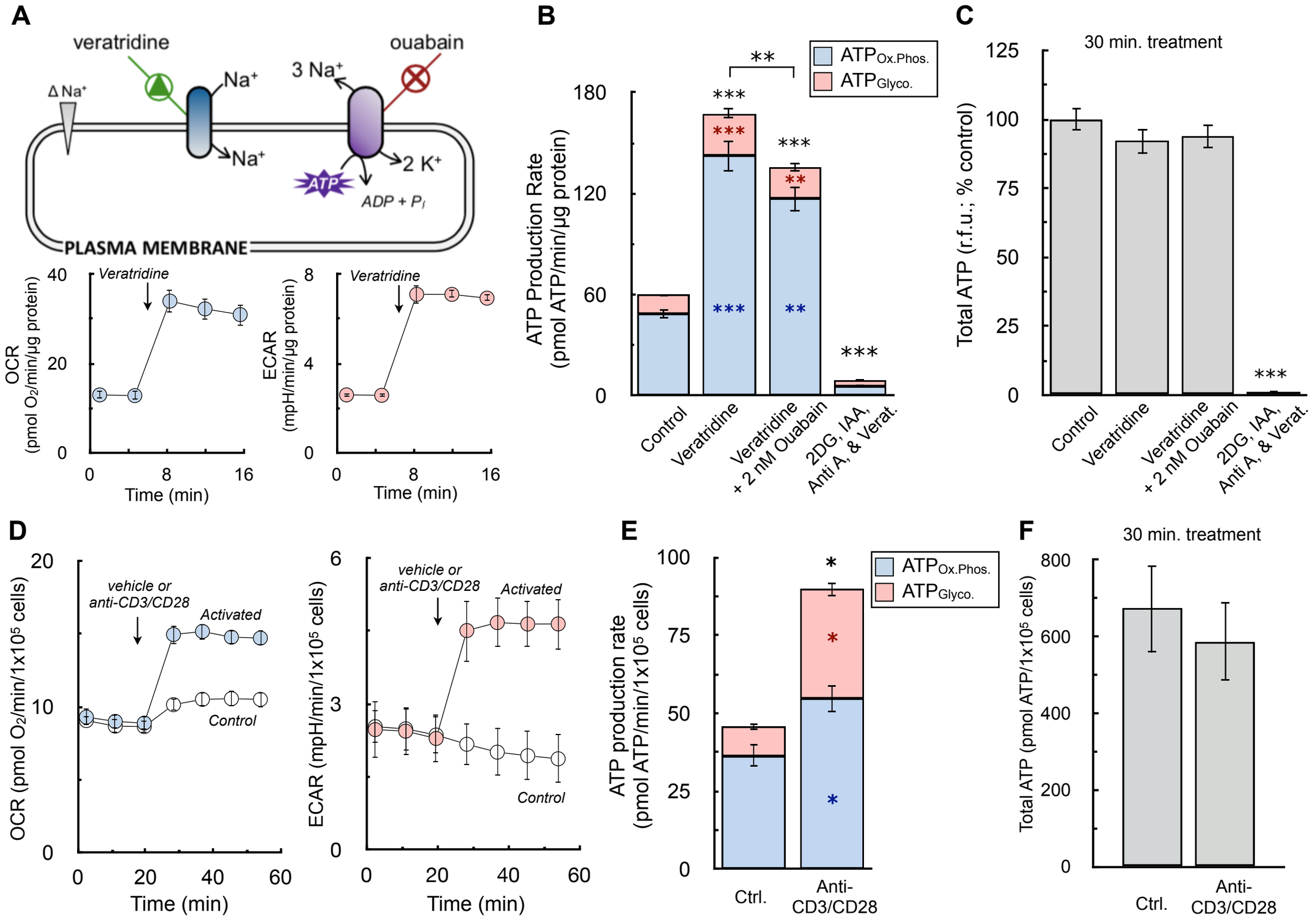
A
veratridine
ouabain
Δ Na+
Na+
3 Na+
Na+
2 K+
ATP
ADP + Pi
PLASMA MEMBRANE
Veratridine
OCR (pmol O2/min/µg protein)
Time (min)
ECAR (mpH/min/µg protein)
B
ATPOx.Phos.
ATPGlyco.
ATP Production Rate (pmol ATP/min/µg protein)
Control
Veratridine
Veratridine + 2 nM Ouabain
2DG, IAA, Anti A, & Verat.
C
30 min. treatment
Total ATP (r.f.u.; % control)
D
vehicle or anti-CD3/CD28
Activated
Control
OCR (pmol O2/min/1x10^5 cells)
ECAR (mpH/min/1x10^5 cells)
Time (min)
E
ATP production rate (pmol ATP/min/1x10^5 cells)
Ctrl.
Anti-CD3/CD28
F
30 min. treatment
Total ATP (pmol ATP/1x10^5 cells)

MANUSCRIPT EXPANDED VIEW

Desousa BR *et al*. "Calculation of ATP production rates using the Seahorse XF Analyzer"

Expanded View Figure 1 – Metabolic reactions that generate net pH changes

(A) The main driver of extracellular acidification in most cell culture monolayer systems is lactate efflux. Uncharged glucose is taken up by the cell and converted to anionic pyruvate via glycolysis. Subsequent fermentation to lactate and efflux via monocarboxylate transporters causes a net pH change in the experimental medium that is detected by the XF Analyzer. GLUT, glucose transporter; MCT, monocarboxylate transporter; PYR., pyruvate; LAC., lactate.

(B) Other reactions can cause a net pH change in the experimental medium, such as the efflux of glucose-derived carbon as anionic pyruvate or CO_2 evolved from the oxidative pentose phosphate pathway (PPP) that ultimately forms bicarbonate and H^+.

(C) CO_2 evolution by mitochondrial dehydrogenases also generates bicarbonate that can be detected by ECAR. CO2 is evolved from various mitochondrial enzymes including isocitrate dehydrogenase (IDH) and the three oxoacid dehydrogenases: pyruvate dehydrogenase (PDH), α-ketoglutarate dehydrogenase (α-KGDH), and the branched chain keto acid dehydrogenase (BCKDH). α-KIC, α-ketoisocaproic acid, the keto acid derivative of leucine.

Expanded View Figure 2 – Sensor coverage of the well plate can explain why lactate:H^+ > 1

All data are mean $\pm$ S.E.M. unless otherwise specified. *, $p<0.05$; **, $p<0.01$

(A) (*Left*) Cutaway image of Seahorse XF microplate and measurement sensor depicting location of the measurement microchamber, cell monolayer, and fluorometric sensor attached to the measurement cartridge. (*Right*) Birds-eye view diagram of the XF microplate well, where the confluent monolayer in drawn in grey, the three plate risers maintaining the uniform volume of the measurement microchamber are drawn in black, and the area covered by the fluorometric sensor is given in pink.

(B) Representative images of wells assayed with an uninterrupted monolayer of cells ("Full well"), wells with cells scraped off the outer rim ("Center"), and wells with cells scraped off the inner portion of the well ("Donut").

(C) OCR and ECAR in A549 cells for the scraping conditions described in (B). (n=4 biological replicates)

(D) The ratio of lactate (measured by enzymatic assay) to H^+ (measured by the XF Analyzer) for the conditions described in (A & B). (n=4 biological replicates)

Expanded View Figure 3 – Cellular substrate preference and non-glycolytic organic acid efflux can affect H^+:O_2 ratios.

All data are mean ± S.E.M. unless otherwise specified. *, p<0.05; **, p<0.01, ***, p<0.001

(A) Sample oxygen consumption kinetic trace for HepG2 cells offered 5 mM pyruvate, 5 mM 2-deoxyglucose (2-DG), and 50 μM iodoacetate (IAA) in the experimental medium. Where indicated, cells were treated with 1 μM UK5099 for 20 min prior to measurements. (n=10 technical replicates)

(B) Sample H^+ production rates for the conditions as in (A). (n=10 technical replicates)

(C) The H^+:O_2 ratio is given for pyruvate and glutamine oxidation. Rates of H^+ and O_2 production for pyruvate oxidation were calculated as the UK5099-sensitive, maximal rates of respiration & acidification as indicated by the grey brackets in (A & B). Rates for glutamine oxidation were calculated similarly except 5 mM glutamine was offered instead pyruvate in the experimental medium, and the glutaminase inhibitor CB-839 was used instead of UK5099. (n=4 biological replicates)

(D) Sample kinetic traces of oxygen consumption (*left*) and H^+ production (*right*) for rat heart mitochondria offered 10 mM pyruvate with 1 mM malate and 2 mM dichloroacetate (P/M), a substrate and inhibitor mix to run a truncated TCA cycle consisting of P/M supplemented with 60 μM fluorocitrate (to block isocitrate dehydrogenase), 2 mM malonate (to block succinate dehydrogenase), and 1 mM aminooxyacetate (to block transaminase activity) (P/M truncated), or 10 mM succinate with 2 μM rotenone (S/R). All respiration measurements were made in the presence of 2 μM oligomycin and 4 μM FCCP, and background rates were calculated in response to 200 nM rotenone and 1 μM antimycin A. (n=20 technical replicates)

(E) The H^+:O_2 ratio is calculated for each condition as in (D). (n=6 biological replicates)

(F) (*Left*) Oxygen consumption rates in rat heart mitochondria offered conditions as in (D) for P/M truncated assayed in both the XF24 and XF96 assay platforms. (n=5 biological replicates) (*Right*) Measured H^+ production rates for conditions as before (closed bars), compared to the theoretically predicted value assuming every mol of acid is stoichiometrically read by the instrument's H^+ sensor (open bars).

(G) Primary cortical neurons are offered 5 mM β-hydroxybutyrate in aCSF medium supplemented with 5 mM 2-DG, and 50 μM IAA. Where indicated, cells were acutely treated with 100 μM

NMDA or NMDA plus the NMDA receptor inhibitor MK-801 (10 μM). (n=10 technical replicates)

(H) The H^+:O_2 ratio is calculated for each condition as in (F). (n=4 biological replicates)

(I) The lactate efflux rate as measured by enzymatic assay for neurons treated for 20 min with the conditions as in (F). (n=3 biological replicates)

Expanded View Figure 4 – Changes in proportion of organic acid efflux during cell activation.

All data are mean ± S.E.M. unless otherwise specified. *, p<0.05; **, p<0.01, ***, p<0.001

(A) Sample oxygen consumption kinetic trace for iBAT cells offered 10 mM glucose, 2 mM glutamine, and 2 mM pyruvate in the experimental medium. Where indicated, cells were treated with 2 μM oligomycin or 200 nM rotenone with 1 μM antimycin A. NE = 5μM norepinephrine. (n=10 technical replicates)

(B) Sample kinetic trace of the H^+ production rate as in (A). (n=10 technical replicates)

(C) Rates of basal mitochondrial respiration rates and respiration associated with proton leak for conditions as in (A). (n=3 biological replicates)

(D) Lactate efflux rates calculated by either the Seahorse XF Analyzer or an enzymatic lactate assay as described in the manuscript methods. NE, as before. (n=3 biological replicates)

(E) Fold-change in lactate efflux in response to norepinephrine as measured by the Seahorse XF Analyzer or an enzymatic lactate assay. NE, as before. (n=3 biological replicates)

Expanded View Figure 5 – Images of well plate after 24 hr. LPS treatment

All data are mean ± S.E.M. unless otherwise specified. *, p<0.05; **, p<0.01, ***, p<0.001

(A) BMDMs were plated at $5x10^4$ cells/well treated with 50 ng/mL LPS for 24 hr. in Seahorse XF96 well plates. (A) After the assay, cells were fixed overnight with 2% (v/v) paraformaldehyde, stained with Hoescht 33342, and images were captured using the Perkin Elmer Operetta.

(B) Quantification of cell counts after 24 hr. treatment with LPS. (n=4 biological replicates)

Expanded View Figure 1

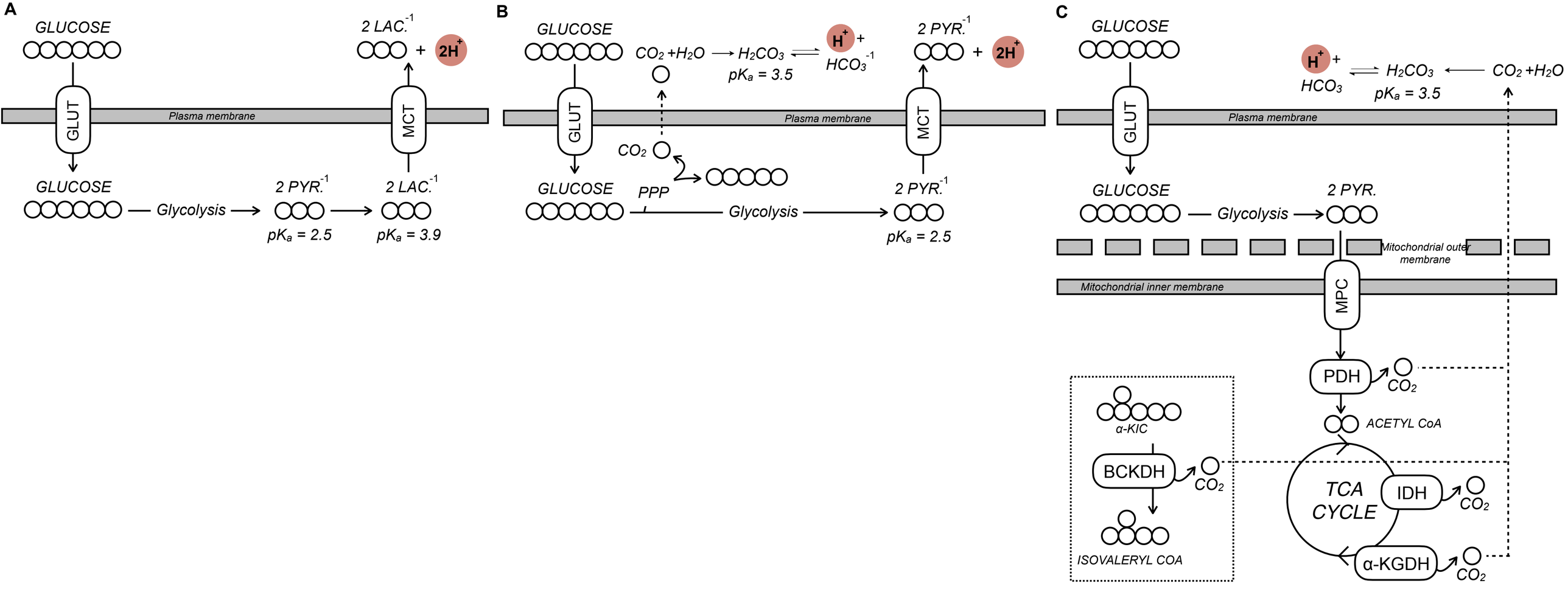

Expanded View Figure 2

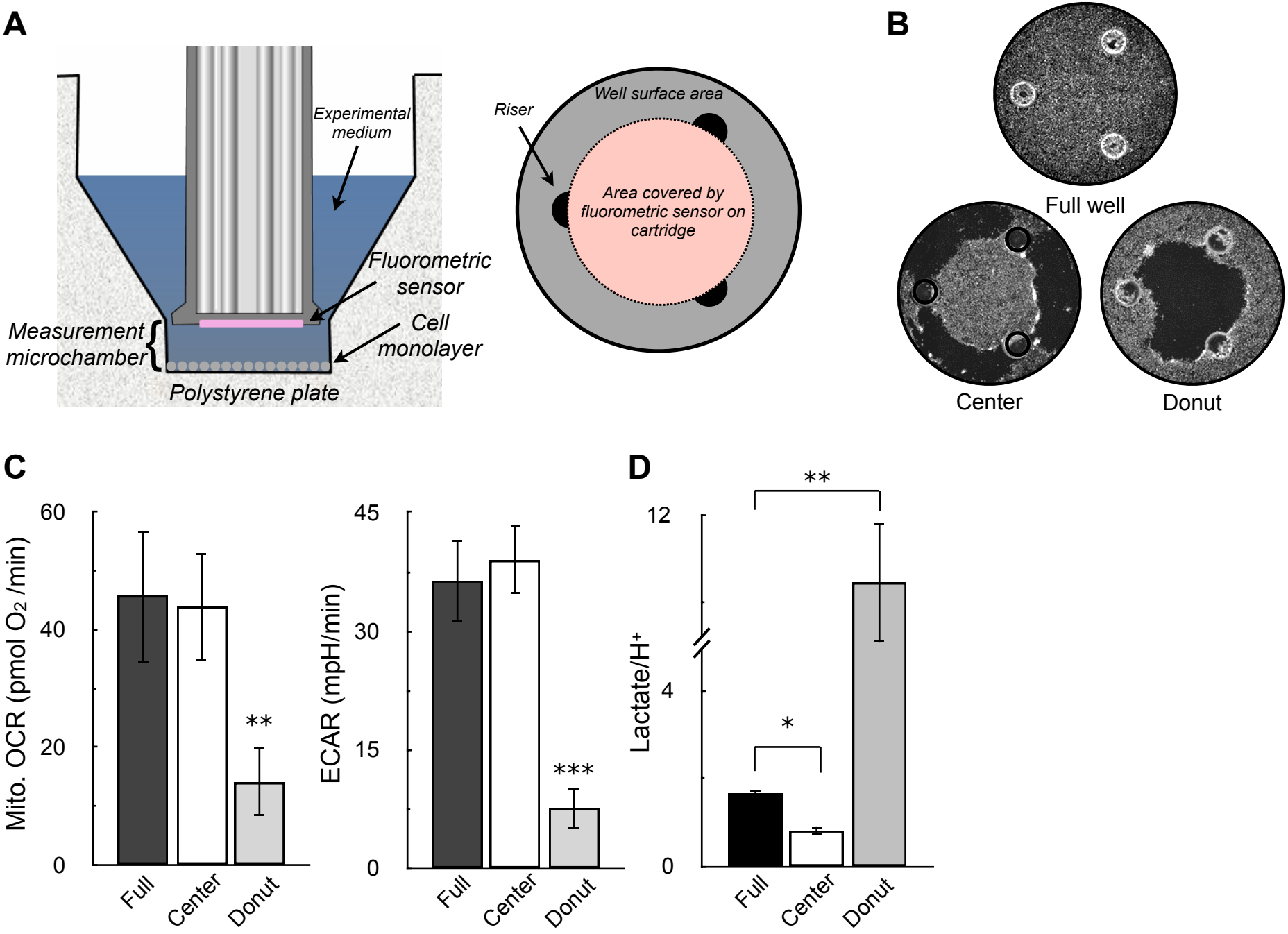

Expanded View Figure 3

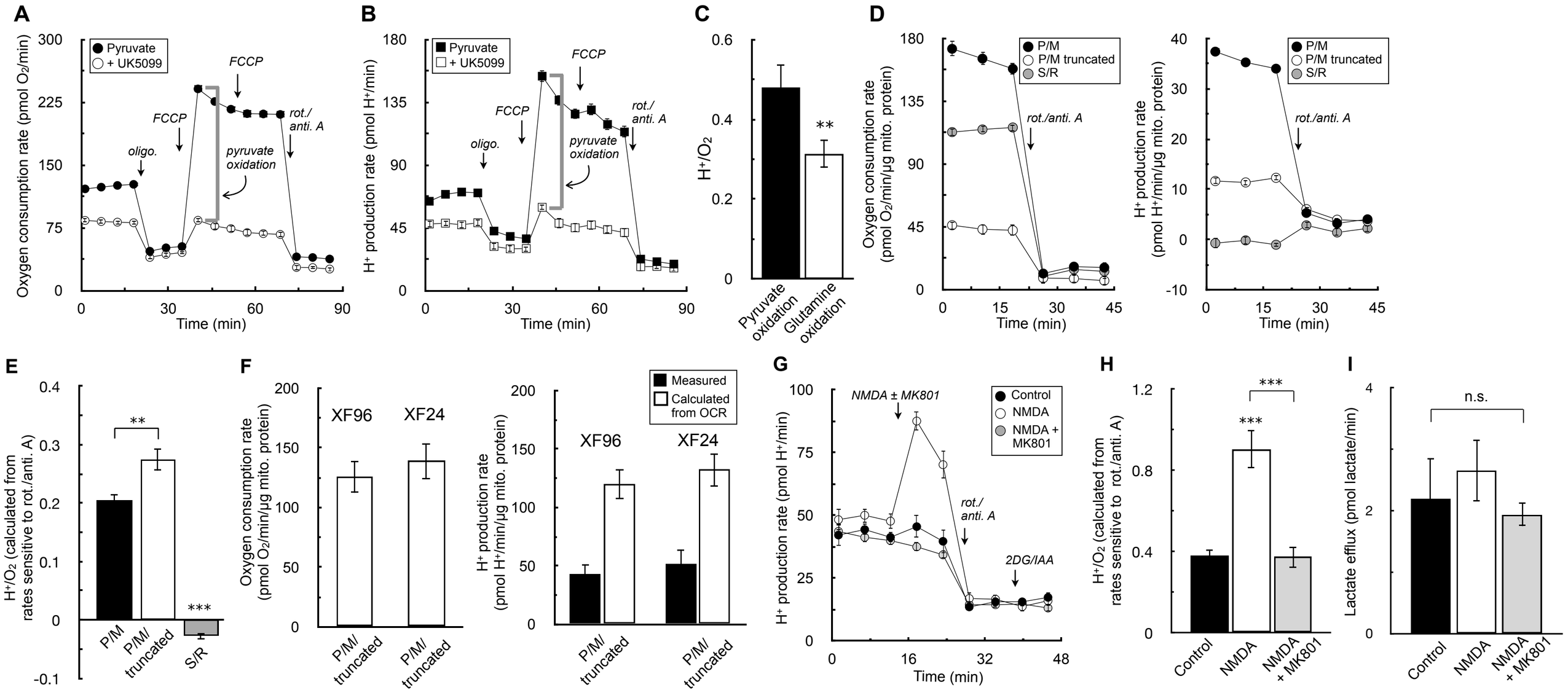

Expanded View Figure 4

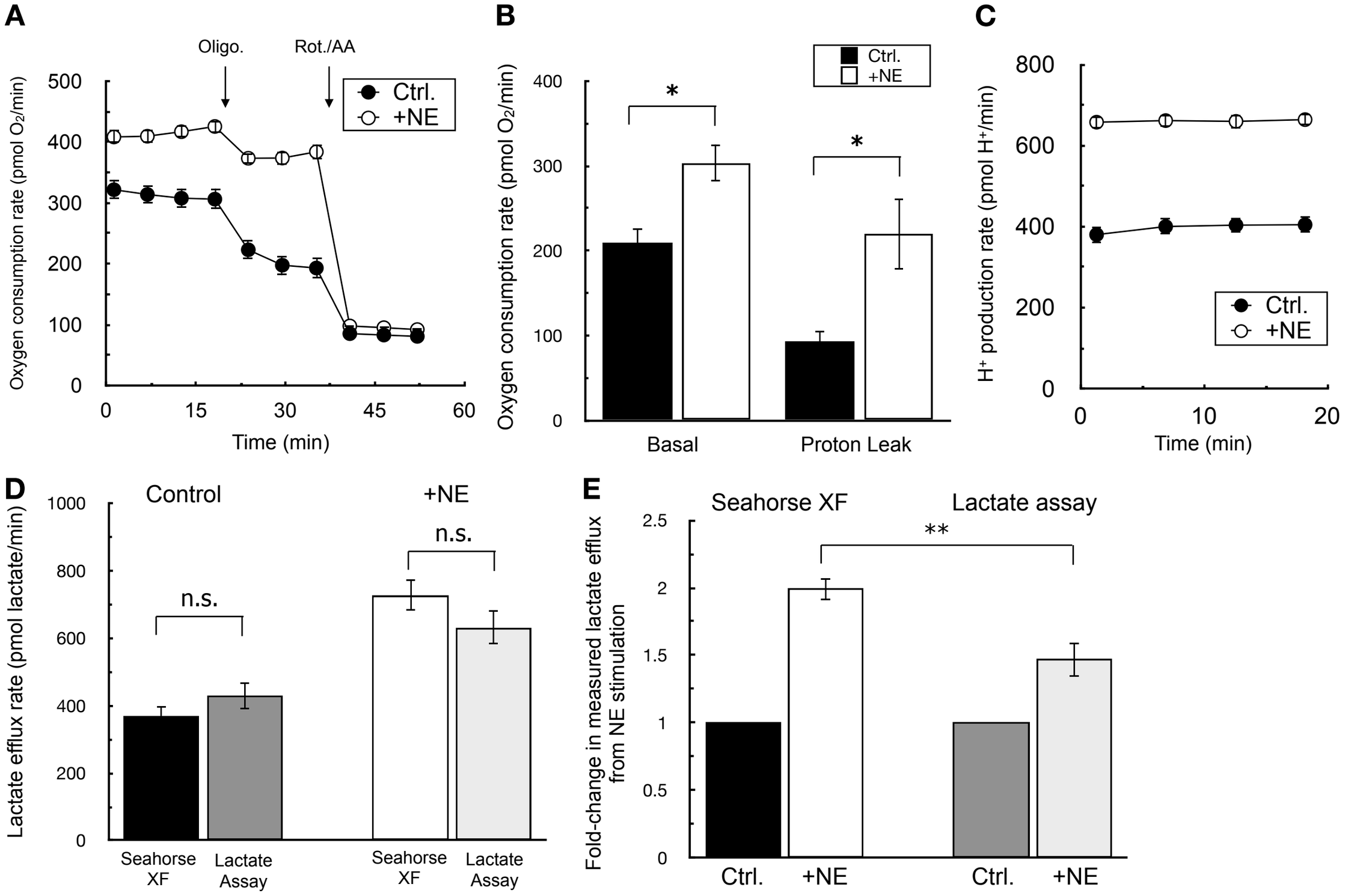

Expanded View Figure 5

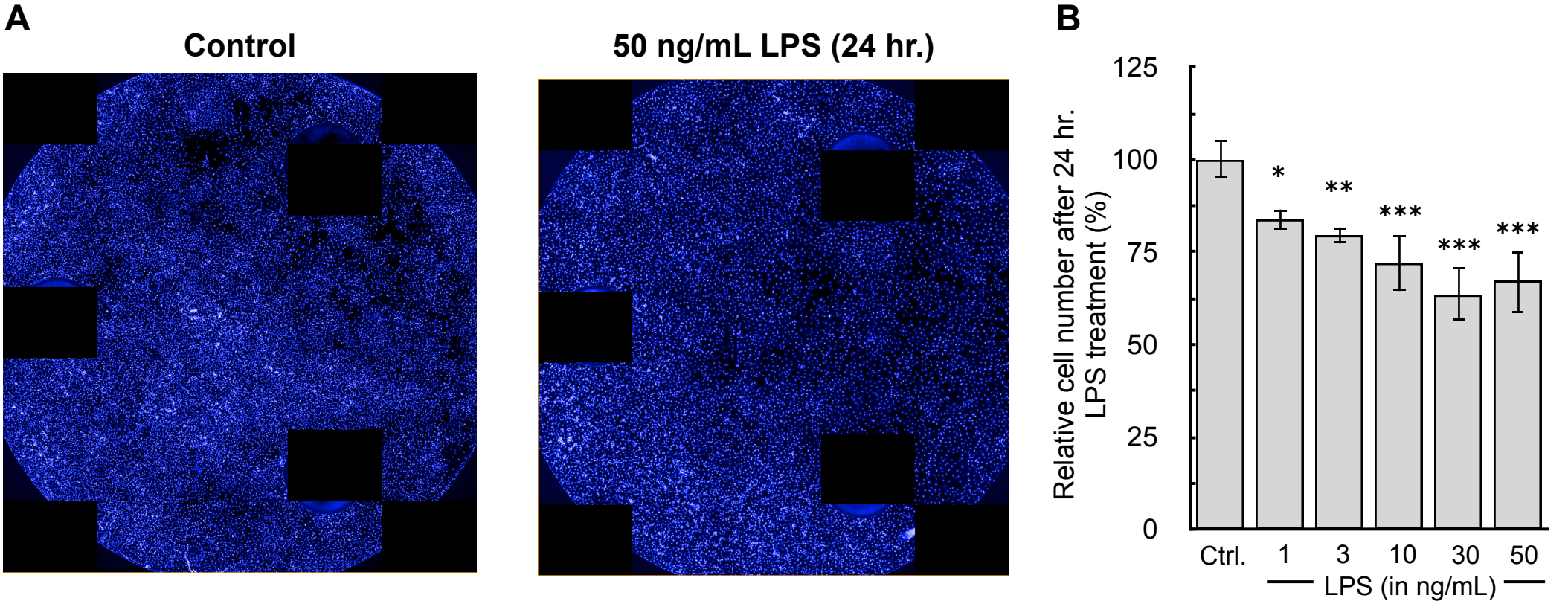

Appendix Table 1: Lactate:H^+ values used for composite factor

Cell Type	Lactate:H+
3T3-L1	1.73
A431	1.28
A549	1.60
BAEC	1.58
BMDM	1.58
BT474	1.51
C2C12	1.46
Cortical neuron	1.45
H460	1.58
HCT116	1.43
HepG2	1.36
HUVEC	1.55
Jurkat	1.54
MCF10A	1.64
MDA-MB231	1.61
PC12	1.74
Raw 264.7	1.45
Average	**1.53**
St. Dev.	**0.12**

Appendix Table 2: H^+:O_2 values used for composite factor

Cell Type	H+/O2
3T3-L1	0.40
A431	0.35
A549	0.39
BAEC	0.34
BMDM	0.47
C2C12	0.33
Cortical astrocyte	0.43
Cortical neuron	0.49
H460	0.40
HCT116	0.35
HepG2	0.36
HUVEC	0.45
INS-1	0.34
Jurkat	0.38
MCF10a	0.31
MCF7	0.35
MDA-MB231	0.38
NRVM	0.33
PC12	0.41
RAW 264.7	0.28
Splenocytes	0.35
AVERAGE	**0.38**
St. Dev.	**0.05**